

Unveiling the coupling effect of sp^2 domain size and local active sites in switching the selectivity of nanocarbon catalysts toward the oxygen electro-reduction

Received: 26 January 2025

Accepted: 29 October 2025

Published online: 16 December 2025

Check for updates

Chaowei Yang^{1,2}, Fei Sun^{1,2} , Yi Zhang^{1,2}, Zhibin Qu^{1,2}, Jiayu Zuo^{1,2}, Wei Zhou^{1,2}, Jihui Gao^{1,2}, Shaoqin Liu³ & Yunfeng Lu^{1,2,4}

Carbon-mediated active site engineering has demonstrated remarkable electrocatalytic activities for oxygen reduction reactions (ORR), yet the relationship between carbonaceous structure and ORR selectivity remains unclear. Herein, we show that local active sites and sp^2 domain size jointly regulate ORR selectivity. Specifically, we demonstrate that while local active sites determine the rate-limiting intermediate type (from O_2^{*} to OOH^*), increasing sp^2 domain size can either promote OOH^* formation and subsequent O-O bond dissociation or facilitate OOH^* consumption to enhance the reaction rate, all of which enable the ORR pathway to switch from $2e^-$ to $4e^-$. This coupling is also validated using nitrogen-doped carbon soot to induce a profound change in ORR selectivity, where the synergistic interplay between small carbon domain sizes and nitrogen dopants boosts the $2e^-$ selectivity from ~50% to over 90%. Ultimately, p -band theory integrates these coupling mechanisms, offering a fundamental principle for designing highly selective nanocarbon electrocatalysts.

Carbon-catalyzed oxygen electroreduction reactions, owing to the diversity of carbon nanostructures, exhibit highly adjustable electron transfer properties that 4-electron transfer ($4e^-$ pathway: $O_2 + 4H^+ + 4e^- \rightarrow 2H_2O$) can be used for energy conversion devices like fuel cells, while 2-electron transfer can be employed for the efficient synthesis of hydrogen peroxide ($2e^-$ pathway: $O_2 + 2H^+ + 2e^- \rightarrow H_2O_2$)^{1,2}. To guide the design and regulation of high-performance carbon electrocatalysts towards designated oxygen reduction reaction (ORR), it is crucial to understand the origins of both electrocatalytic activity and selectivity of carbon catalysts^{3,4}. In the past decade, an increasing amount of research has demonstrated that ORR activity can be enhanced via active site engineering, such as defects^{4,5}, heteroatom dopants (such as Boron doping^{6,7}, Nitrogen doping¹⁻³ and Oxygen doping⁸⁻¹⁰), and porous nanostructures^{11,12} of carbon catalysts (Supplementary Fig. 1);

however, these reported carbon structures are either used for the $2e^-$ ORR or the $4e^-$ ORR pathway, and the exact nature of active units in carbon catalysts that determine ORR selectivity remains elusive due to the complex electronic and surface structures of carbon catalysts from different precursors and synthetic methods. Therefore, compared to a large number of reported studies on activity enhancement, there is still much work remaining to be done toward identifying the structure-selectivity relationship, particularly with regard to experimentally designing controllable carbon nanostructures to efficiently switch the ORR selectivity^{13,14}.

Based on the general consensus of active site engineering for carbon-based catalysts, the local electron transfer between atomic-scale functional units (e.g., dopants, edges, defects) and neighboring carbon atoms breaks the delocalization of the π -conjugated carbon

¹School of Energy Science and Engineering, Harbin Institute of Technology, Harbin, China. ²National Innovation Platform for Industry-Education Integration of Energy Storage Technology, Harbin, China. ³School of Medicine and Health, Harbin Institute of Technology, Harbin, China. ⁴Beijing Advanced Innovation Center for Soft Matter Science and Engineering, College of Materials Science and Engineering, Beijing University of Chemical Technology, Beijing, China.

e-mail: sunf@hit.edu.cn

lattice system, thus generating active carbon sites with highly localized electronic states for ORR^{15–17}. This indicates that the generation of high-performance active sites is closely related to both local electron transfer and global electron delocalization characteristics of carbon framework. From this perspective, in addition to the local electron transfer mediated by well-studied atomic-scale structural units, the nano-sized sp^2 carbon domains (π -conjugated basal planes or microcrystals) may also play a crucial role during the ORR process, as their size growth governs the degree of electron delocalization. However, there is limited exploration on the size effect of carbon catalysts in the field of electrocatalysis to date. Among the few investigations, Li¹⁸ and colleagues pioneered the study of size-dependent ORR activity through the synthesis of nitrogen-doped graphene quantum dots (GQDs) and showed that the ORR activity rises with the augmentation of quantum dot size. Conversely, Woo¹⁹ et al. demonstrated that ball milling can improve ORR activity by reducing the size of nitrogen-doped graphene. In particular, this study found that reducing the dimensions of graphene leads to higher Fermi level and improves electron transfer kinetics, suggesting that the size effect could critically regulate interfacial electron transfer during ORR process. McCloskey and colleagues²⁰ have also shown that changes in the carbon hybridization state of graphene oxide can affect the electron density at the Fermi level and thereby impact ORR activity and selectivity. Intrinsically, sp^2 carbon domain and local active sites serve as the fundamental functional units of carbon catalysts and may collectively affect the electron transfer behavior during the ORR process, thereby changing the adsorption strength and bond-breaking characteristics of reaction intermediates. Nevertheless, previous limited studies on the size effect and sp^2 hybridization states of carbon catalysts have primarily focused on ORR activity, while the structure-selectivity relationship in carbon catalysts, particularly the coupling effect of sp^2 carbon domain size and local active sites on ORR selectivity, has not been reported. In fact, during the carbon catalyst preparation and modification processes, unavoidable factors such as uneven heating can lead to heterogeneous sizes of the π -conjugated system even within the same batch of nanocarbon. Due to the limitations associated with controllably preparing model carbon catalysts with global sp^2 domain sizes, the origin of ORR selectivity for nanocarbon, jointly governed by atomic-scale functional units and nanoscale carbon domain size, remains poorly understood^{3,9}.

Herein, we uncover an underlying coupling mechanism between sp^2 domain size and local active sites in carbon catalysts that enables the switching of ORR selectivity towards either $2e^-$ or $4e^-$ pathways. By designing model carbon catalyst systems with tunable sp^2 domain size and local active sites, combined with reliable statistical learning (partial least squares regression, F -tests, and linear regression), we find that increasing the carbon domain size enables ORR selectivity switching from $2e^-$ to $4e^-$ pathway for both simple graphene quantum dots and amorphous carbons. This research strategy, integrating model catalysts with statistical learning, provides a powerful framework for deconvoluting the complex structure-activity relationships within catalytic systems. Furthermore, by combining in situ electrochemical surface-enhanced Raman spectroscopy (SERS) and multiscale theoretical calculations (DFT, AIMD, and microkinetic simulations), we demonstrate that while local active sites determine the rate-limiting intermediate type (from O_2^* to OOH^*), increasing the sp^2 domain size can either promote OOH^* formation and subsequent O-O bond dissociation (undoped, armchair-edge, and pyridinic/pyrrolic N-doped cases) or facilitate OOH^* consumption to enhance the reaction rate (graphitic N-doped, cyclic ether, carbonyl, and multiple nitrogen co-doped cases). These synergistic behaviors were further validated by using nitrogen-doped carbon soot catalysts to induce a profound change in the ORR reaction pathway and selectivity from $\sim 50\%$ to over 90% . The revealed coupling effect of the carbon catalyst aligns well with the p -band theory, wherein size variations regulate the filled states

of the p -band below the Fermi level or p -band center gaps between spin-up and spin-down states, thereby governing the formation, bond-breaking, and desorption behaviors of rate-limiting intermediates in selective ORR pathways.

Results

Structure-dependent ORR selectivity of nanocarbons

Figure 1a illustrates the typical ternary phase diagram corresponding to carbon hybridization forms and the clustering degree (or size) of the sp^2 carbon phase, where finite-sized sp^2 carbon domains (carbon basal planes or microcrystals) are critical structural features for both nanocarbons and amorphous carbons. Essentially, variations in the size of sp^2 carbon domains can alter electronic delocalization and the distribution of active sites, implying a potential synergy between the global carbon domain size and local active sites in regulating carbon-based electrocatalysis. Considering that previous explorations of size effects have predominantly focused on nitrogen-doped nanocarbon catalysts^{18–20}, nitrogen-doped graphene quantum dots were initially chosen as model carbon materials to investigate the coupling effect in our study for comparative purposes. To probe the influence of sp^2 domain size that is often intrinsically heterogeneous even within a single batch of catalysts, a chemical cutting method was employed for sample preparation. Crucially, size modulation was achieved through the nanoscale sieving of quantum dots originating from the identical batch according to the previous research²¹ (Supplementary Figs. 2–4, see “Methods” section for more details). As expected, transmission electron microscope (TEM) images of three types of graphene quantum dots clearly exhibit differences in size at the same magnification (Fig. 1b–d). Statistical analysis from the TEM images yields average sizes of ~ 2.37 nm, 2.75 nm, and 4.44 nm for the small (S-GQDs), medium (M-GQDs), and large (L-GQDs) quantum dots, respectively (Fig. 1e–g). Typical high-resolution TEM (HRTEM) images further illustrate a lattice spacing of 0.376 nm (Fig. 1h–j) that corresponds to the (002) carbon facet. The size variation characteristics obtained by TEM are also corroborated in both ultraviolet-visible (UV-vis) absorption and Raman spectroscopy. Specifically, UV-vis absorption spectra were measured to estimate the optical band gap of prepared GQDs through the Tauc equation (Supplementary Fig. 5)^{22–24}. As shown in Fig. 1k, the band gap gradually decreases from 4.61 eV to 4.49 eV with increasing the GQD size, confirming the influence of quantum size effects on the energy band structure of quantum dots^{25,26}. Raman spectra were also used to estimate the average size of sp^2 carbon domain (L_a). For materials like nanocrystalline graphite or GQDs, their inherently small size and significant edge-to-area ratio lead to the breakdown of the conventional TK relationship ($I_D/I_G \propto 1/L_a$). In this case, L_a is known to scale with $\sqrt{I_D/I_G}$, where I_D and I_G are the intensities of the D and G Raman bands, respectively^{20,27}. Figure 1l depicts the statistical distribution of $\sqrt{I_D/I_G}$ through a multi-point test for three samples. The average values of $\sqrt{I_D/I_G}$ are 0.81 , 0.92 , and 0.98 for S-GQDs, M-GQDs, and L-GQDs, respectively (Supplementary Fig. 6), indicating a gradual increase in domain size from S-GQDs to L-GQDs.

It is well-established that surface chemistry (e.g., nitrogen and oxygen dopants) and crystalline structure (e.g., the sp^2 and sp^3 distribution) are intimately linked with ORR kinetics^{8,9,28–31}. Therefore, to understand the interplay between these properties and the intrinsic size effect, the surface composition and carbon structure of our GQD samples were meticulously characterized. Because the three GQDs samples were derived from the same sample batch, they exhibited largely consistent nitrogen (6.8 – 7.3 at.%) and oxygen contents (20 – 25 at.%) as shown in Supplementary Fig. 7, which was validated across two independent X-ray photoelectron spectroscopy (XPS) measurements. High-resolution N 1s and C 1s spectra in Fig. 1m, n and Supplementary Fig. 8 further confirm that the GQDs of various sizes possess

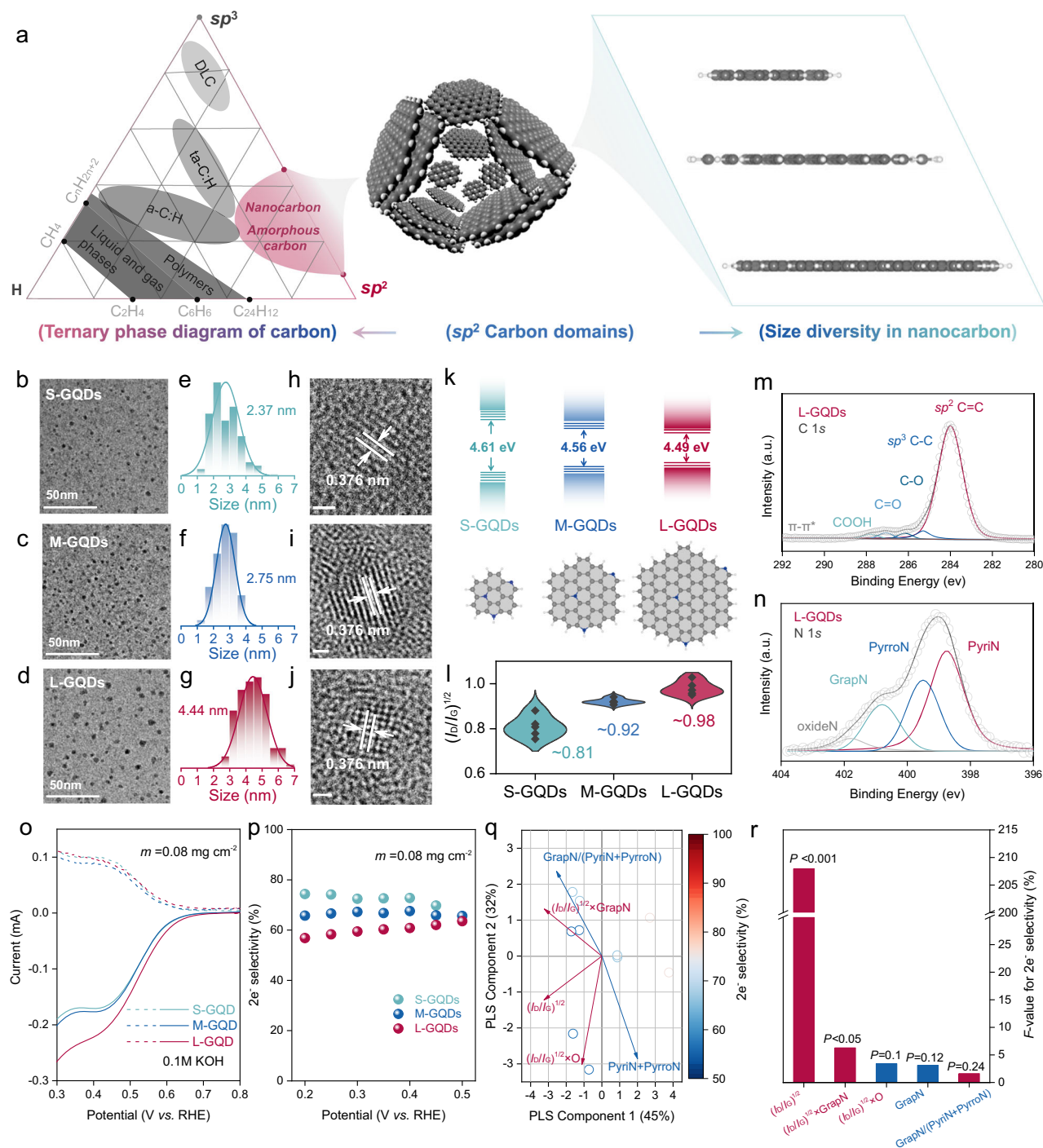


Fig. 1 | Structural characterization, ORR performance, and statistical analysis of GQD catalysts. **a** Schematic of size effects for sp^2 carbon domains, where black and white spheres in the molecular models represent carbon and hydrogen atoms, respectively. Typical TEM images (**b–d**), the size distribution (**e–g**), and HRTEM images (**h–j**) of S-GQDs, M-GQDs, and L-GQDs (from top to bottom). Scale bar: 50 nm for (**b–d**) and 2 nm for (**h–j**). **k** Schematic illustration of the band gap and structure of S-GQDs, M-GQDs, and L-GQDs. **l** Statistical distribution of the Raman intensities of D bands (I_D) and G bands (I_G) for S-GQDs, M-GQDs, and L-GQDs in multiple point tests. **m, n** High-resolution C 1s and N 1s XPS spectra of L-GQDs, respectively. **o** RRDE polarization curves (solid lines) and corresponding ring currents (dashed lines) for the three GQD catalysts without iR-compensation. Measurements were performed in an O_2 -saturated (200 sccm) 0.1 M KOH electrolyte at 25 °C, with a scan rate of 10 $mV s^{-1}$ and a rotation speed of 1600 r.p.m. **p** Calculated $2e^-$ selectivity (H_2O_2 selectivity) of three GQDs during the potential sweep. **q** Partial least squares regression (PLSR) bi-plot showing the scores (dots) and loadings (vectors) for ORR selectivity. The percentages on the axes indicate the variance explained in the input features (X-variables), while the model as a whole explains 87% of the total variance in ORR selectivity. **r** F -test results illustrating the statistical significance of various structural descriptors on H_2O_2 selectivity ($P < 0.05$ is considered significant). Source data for (**l–r**) are provided as a Source Data file.

comparable configurations. Specifically, all samples feature similar distributions of nitrogen species, including pyridinic N (PyrIN, 398.9 eV), pyrrolic N (PyrroN, 399.5 eV), graphitic N (GrapN, 401.2 eV), and oxidized N (401.9 eV)^{3,32,33}. Similarly, the high-resolution C 1s spectra further reveal a consistent distribution of carbon bonding states^{8,9}, which can be deconvoluted into sp^2 C=C (284 eV), sp^3 C-C (285 eV), C-O (286 eV), C=O (287 eV), and the characteristic $\pi-\pi^*$ shake-up satellite peak at 291.2 eV. This compositional similarity is further

corroborated by Fourier-transform infrared spectroscopy (FTIR) (Supplementary Fig. 9).

With the above detailed structure characterizations, the rotating ring disk electrode (RRDE) technique was employed to evaluate the ORR activity and selectivity. As shown in Fig. 1o, the three types of GQDs display comparable ORR activity in RRDE polarization curves, yet significant differences in selectivity are observed (Fig. 1p). Supplementary Fig. 10 further summarizes the trend of selectivity with GQDs size variation from which the selectivity for the $2e^-$ pathway decreases from ~80 to 50% as the size increases due to more efficient charge transfer. Building on these findings, the complex structure-performance relationships among key carbon features (sp^2 domain size, N/O surface composition, and crystalline structure) and ORR selectivity were further quantitatively investigated using robust statistical analyses, including partial least squares regression (PLSR) and F -tests. Herein, PLSR was employed to reduce the dimensionality of the complex catalytic dataset (carbon structural parameters) and to quantify the contribution of each explanatory variable to the ORR performance; meanwhile, the F -test was used to evaluate the statistical significance of these explanatory variables for the performance metrics^{34,35}. Specifically, our PLSR model incorporated key parameters including sp^2 domain characteristics (represented by $\sqrt{I_D/I_G}$), nitrogen speciation (GrapN, PyriN+PyrroN, and their ratios), oxygen speciation (O%, total content of C-O and C=O groups), carbon hybridization states ratios (sp^2 C=C, sp^3 C-C) and the interaction terms (representing the coupled effects between the global carbon domain size and local dopants, denoted as $\sqrt{I_D/I_G} \times \text{GrapN}$, $\sqrt{I_D/I_G} \times (\text{PyriN} + \text{PyrroN})$, or $\sqrt{I_D/I_G} \times \text{O}$, as detailed in Supplementary Fig. 11 and Supplementary Table 1). These components explained 87% of the total variances in ORR selectivity, demonstrating their effectiveness in explaining the performance metric. The bi-plot in Fig. 1q further visualizes that the most relevant explanatory variables for ORR selectivity are the $\sqrt{I_D/I_G}$, $\sqrt{I_D/I_G} \times \text{GrapN}$, $\text{GrapN}/(\text{PyriN} + \text{PyrroN})$, $(\text{PyriN} + \text{PyrroN})$ and $\sqrt{I_D/I_G} \times \text{O}$. In this model, L-GQDs (low H_2O_2 selectivity, favoring $4e^-$ pathway) clustered on the negative side of component 1, while S-GQDs (high H_2O_2 selectivity, favoring $2e^-$ pathway) were situated on the positive side. The loading vectors indicated that descriptors such as $\sqrt{I_D/I_G}$ and $\sqrt{I_D/I_G} \times \text{GrapN}$ (both intrinsically linked to the sp^2 domain size) strongly aligned with the direction of L-GQDs, suggesting their significant role in promoting the $4e^-$ reduction pathway. Conversely, variables like PyriN+PyrroN content showed alignment towards S-GQDs, a finding consistent with previous reports on the contribution of nitrogen configurations to ORR selectivity²⁹. To rigorously assess the statistical significance of these observations, F -test analysis was performed on the individual descriptors with H_2O_2 selectivity as the response variable (Fig. 1r and Supplementary Fig. 11). The F -test analysis unequivocally identified the $\sqrt{I_D/I_G}$ and $\sqrt{I_D/I_G} \times \text{GrapN}$ as the most statistically significant factors influencing H_2O_2 selectivity, yielding exceptionally high F value of 208 (probability value, $P < 0.001$) and 6.3 ($P < 0.05$), respectively. In contrast, other variables exhibited considerably lower F values and P values well above the significance threshold ($P > 0.05$). Therefore, this comprehensive statistical analysis strongly demonstrates a significant correlation between sp^2 domain size and associated dopant characteristics (as captured by $\sqrt{I_D/I_G}$ and $\sqrt{I_D/I_G} \times \text{GrapN}$) and the ORR selectivity in these GQD catalysts derived from the same batch, suggesting that this previously overlooked synergistic effect may serve as an important descriptor for regulating ORR selectivity.

Structure-dependent ORR selectivity of amorphous carbon

To further extend the findings derived from GQDs to commercial carbon catalysts, which are commonly characterized by complex amorphous structures with microcrystal size as a key mesoscale feature, it is necessary to synthesize amorphous carbon materials with tunable microcrystal sizes within the same batch. However, the

complexity of amorphous carbon structures often makes controlling of sp^2 domains and heteroatom doping challenging. To address this, drawing inspiration from the formation of diverse nano-sized carbon soot in flames during incomplete combustion²⁶, carbon soot was employed as amorphous carbon catalyst to further explore the potential size effect on ORR process. Figure 2a illustrates the schematic diagram for the preparation of carbon soot with various sp^2 domain (microcrystal) sizes. Specifically, with the increase in flame height during combustion, simple hydrocarbons have the potential to transform into larger molecules, particularly polycyclic aromatic hydrocarbons (PAHs). These larger molecules subsequently aggregate into carbon nanoparticles, which further grow and amalgamate, forming more extensive, fractal-like structures (Supplementary Fig. 12)^{36–38}. As a result, model carbon catalysts with diverse sp^2 domain sizes can be produced by collecting carbon soot from the same flame at different heights during the combustion of a candle flame, denoted as CS-low, CS-middle, and CS-top, respectively. The overlaid fringe mapping in HRTEM images elucidates the evolution of the soot nanostructure at three different heights, clearly signifying that the average size of carbon soot increases with the rise in sampling height (Fig. 2b, *additional details of data processing are provided in* Supplementary Figs. 13–16). To track the size change of carbon domains present within the soot particles, the distribution of the fringe length values was measured and converted into the number of aromatic rings³⁷. As illustrated in Fig. 2c, carbon soot collected at the lowest height retains the highest percentage of low aromatic ring numbers (around 7 aromatic rings). With an increase in sampling height, the proportion of high aromatic ring numbers (around 37 aromatic rings) gradually escalates for CS-top and CS-middle, suggesting that raising the sampling height results in a more significant proportion of larger-sized polycyclic aromatic hydrocarbons (PAHs). In addition to the microcharacterization results obtained through HRTEM, additional insights into the growth of carbon soot nanoparticles have been gained through Raman spectroscopy. As shown in Fig. 2d, an apparent photoluminescence background (PL) is visible that arises from the radiative recombination of electrons and holes in localized states created by sp^2 carbon domains^{39,40}. Previous research has demonstrated that the background photoluminescence in Raman spectra gradually decreases in more mature carbon soot structures⁴⁰. In our carbon soot samples, a similar phenomenon is also observed where the fluorescence background signal noticeably diminished with an increase in sampling height, indicating the presence of more mature structures in CS-top. In addition, larger-sized mature carbon soot also exhibits the a lower optical band gap in UV-vis absorption spectra, a trend similar to that observed for our GQD samples (Supplementary Fig. 17).

Based on the foregoing structural characterizations, it is confirmed that the three types of carbon soot samples, all derived from the same combustion source, indeed possess lattice fringe structures of varying sizes. To further clarify the potential influence of surface chemistry on the ORR activity and selectivity, two independent sets of XPS tests were also conducted to identify the distribution of oxygen groups and the crystalline structure (particularly the sp^3 component in the carbon soot). As shown in Fig. 2e and Supplementary Fig. 18, the three materials exhibit similar total oxygen contents (averaging 3.7–4.7 at.%) and almost no nitrogen elements was detected. Compared to the GQDs, the high-resolution C 1s spectra reveal a significantly lower proportion of sp^2 C=C and a correspondingly higher proportion of sp^3 C-C in the amorphous structure of the carbon soot (Fig. 2e). Meanwhile, the high-resolution O 1s spectra of the three samples were deconvoluted into four distinct regions^{41,42}: I (531.2 eV, C=O related groups), II (532.3 eV, C-O-H/C=OOH), III (533.4 eV, C-OH), and IV (534.2 eV, C-O-C), respectively (Fig. 2f). Crucially, it is clear that the distribution of these oxygen functional groups showed minimal variation among the three carbon soot samples. The ORR performance

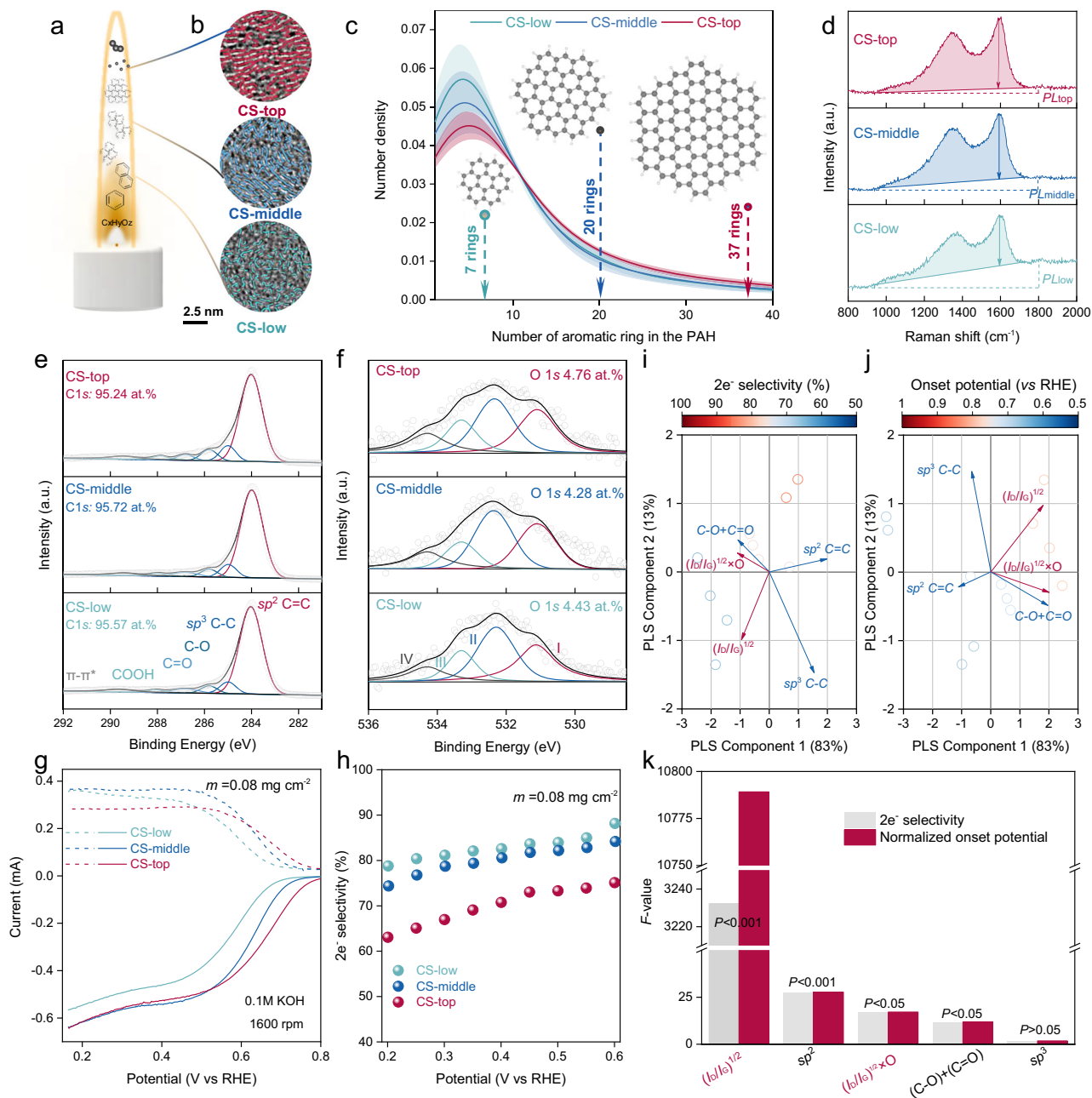


Fig. 2 | Synthesis, structural characterization, ORR performance, and statistical analysis of carbon soot catalysts. **a** Schematic diagram illustrating the principles of preparing carbon soot of different sizes based on the candle flame combustion process. **b** HRTEM images of CS-low, CS-middle, and CS-top (from bottom to top). Scale bar: 2.5 nm. **c** Number density of aromatic rings in three carbon soot samples, with an illustration of the PAH molecules of different sizes, where the black spheres represent carbon atoms. **d** Raw Raman spectra for CS-low, CS-middle, and CS-top. **e, f** High-resolution C 1s and O 1s XPS spectra, respectively. **g** RRDE polarization curves (solid lines) and corresponding ring currents (dashed lines) for three carbon soot samples without iR-compensation. Measurements were

performed in an O₂-saturated (200 sccm) 0.1M KOH electrolyte at 25 °C, with a scan rate of 10 mV s⁻¹ and a rotation speed of 1600 r.p.m. **h** Calculated 2e⁻ selectivity (H₂O₂ selectivity) of three carbon soot samples during the potential sweep.

i, j Partial least squares regression (PLSR) bi-plots for H₂O₂ selectivity and onset potential, respectively. The percentages shown on the axes correspond to the variance explained in the predictor variables (X-variables), while the resulting models explain 97% and 96% of the total variance in H₂O₂ selectivity and onset potential, respectively. **k** F-test results illustrating the statistical significance of various structural descriptors on H₂O₂ selectivity and onset potential ($P < 0.05$ is considered significant). Source data for (c–k) are provided as a Source Data file.

tests of the three model carbon soot samples were then evaluated in basic environments similar to the GQDs samples. As illustrated in Fig. 2g, the three carbon soot catalysts exhibit distinctive reaction characteristics that larger-sized carbon soot displays reduced interfacial electron transfer impedance and higher ORR activity (Supplementary Fig. 19), with corresponding defect-normalized onset potentials enhanced from 0.68 V for CS-low to 0.73 V and 0.77 V for CS-middle and CS-top, respectively^{4,43,44}. More importantly, increasing

the sp^2 domain size of carbon soot leads to a decrease in 2e⁻ORR selectivity from 85% to 60%, signifying the gradual transition of ORR selectivity from the 2e⁻ to 4e⁻ pathway (Fig. 2h). It is noteworthy that differences in surface roughness and double-layer capacitance among the three carbon soot catalysts could potentially lead to the reduction of H₂O₂ to H₂O during its diffusion from the disk to the ring electrode^{45,46} (Supplementary Fig. 20). To correct for the potential impact of this quasi-four-electron reduction (2 + 2e⁻ pathway) on ORR

selectivity, H₂O₂ reduction voltammetry was conducted separately to evaluate the rate constant of the H₂O₂ reduction, as shown in Supplementary Figs. 21–22. After this correction, the trend of H₂O₂ selectivity with varying *sp*² domain size remained unchanged, and the 2e⁻ selectivity of the small-sized catalyst could reach 95–100%.

Building upon these findings, detailed PLSR and *F*-test analyses were conducted again to reveal the complex structure-performance relationships for amorphous carbon soot (Supplementary Table 2). As can be seen in Fig. 2i–k, the resulting PLSR models demonstrated strong predictive power, explaining 97% and 96% of the total variance in H₂O₂ selectivity and onset potential, respectively. In these bi-plots, the sample scores are clearly separated along component 1 and the loading vectors in both models show that the $\sqrt{I_D/I_G}$ strongly aligns with the high 4e⁻ selectivity samples (corresponding to higher onset potential and lower H₂O₂ selectivity). The *F*-test also identified $\sqrt{I_D/I_G}$ as the most statistically significant factor for both H₂O₂ selectivity ($F = 3232, P < 0.001$) and onset potential (normalized by defect density, $F = 10789, P < 0.001$) in Fig. 2k. Moreover, the interaction term $\sqrt{I_D/I_G} \times O$ also showed statistical significance ($P < 0.05$), indicating a potential synergistic relationship between the *sp*² domain size and oxygen doping for the influence on the overall catalytic performance. In contrast, descriptors related to the single *sp*³ component in this amorphous carbon soot system were found to be statistically insignificant ($P > 0.05$). In conclusion, based on the observed trend of ORR activity and selectivity, it implies that the intrinsic size of carbon structures, in synergy with surface chemistry, is a crucial factor for tuning ORR selectivity, whether for relatively simple nitrogen-doped graphene quantum dots or complex amorphous carbons.

Multiscale theoretical calculations

So far, by designing two types of carbon catalysts with a gradient in *sp*² domain size, we have demonstrated that *sp*² domain size not only influences catalytic activity but also plays a pivotal role in altering ORR selectivity, where an increase in size tends to shift selectivity from the 2e⁻ pathway to the 4e⁻ pathway. To elucidate the potential coupling effects of the overall crystalline size with local doping and edge defects on ORR selectivity, multiscale theoretical calculations, including density functional theory (DFT), ab initio molecular dynamics (AIMD), and microkinetic simulations, were employed to investigate the reaction thermodynamics and kinetics. Carbon cluster models with three types of *sp*² domain sizes were first established based on the actual microcrystal sizes (*L*_a) of our carbon soot catalysts extracted from HRTEM images in Fig. 2c. The corresponding undoped pristine carbon model is shown in Fig. 3a, and five distinct nitrogen configurations (basal-plane graphitic-N, edge graphitic-N, pyridinic N, pyrrolic N, and multi-N doping), two oxygen configurations (epoxide and carbonyl), and an armchair-edge-terminated configuration are all considered in conjunction with the real carbon structure to reveal the coupling effects of finite size, edge structure, and heteroatom dopants (Supplementary Figs. 23, 24 and Supplementary Data 1). In these computational models with different sizes, the random distribution of active sites near the dopant or dispersed along the distant edges often results in significant discrepancies in the calculated results due to the improper selection of active sites for the computations^{47,48}. To accurately identify the active sites in these carbon models, our previous studies⁴⁹ have revealed that the activity trends of finite-sized aromatic carbon clusters can be accurately described by the Radical Fukui function, which measures the response of local electron density to changes in electron number within a molecular system. Compared to pyridinic-N-type models (pyridinic N, pyrrolic N, armchair-edge, and pristine models), graphitic-N-type models (graphitic-N and oxygen-doped models) can introduce additional spin-polarized states into the carbon framework and generate localized unpaired electrons, which may lead to a different coupling mechanism between the size effect and doping^{50,51}. Therefore, the Radical Fukui function analysis for these two categories

of models was conducted separately. Based on this, small-sized graphitic N and pyridinic N models were selected as representatives to correlate the adsorption free energy of the key OOH* intermediate with the Radical Fukui function. For the pyridinic-N-type models (Fig. 3b and Supplementary Figs. 25–28), although higher Fukui function values correlated with stronger OOH* adsorption, all potential sites ultimately exhibited weak adsorption ($\Delta G_{\text{OOH}^*} > 4.2$ eV). Consequently, the site with the highest Radical Fukui function was selected as the representative active site. In contrast, the graphitic-N-type models consistently possessed a few strong adsorption sites ($\Delta G_{\text{OOH}^*} < 4.2$ eV) with high Fukui function values near the edges and heteroatoms (Fig. 3c and Supplementary Figs. 29–33). Given their distinct nature, all these strong-adsorption sites were incorporated into the subsequent calculations.

Following the computational framework established above, the free-energy diagrams of the competing 2e⁻ and 4e⁻ pathways for all models are illustrated by volcano plots depicting the relationship between the thermodynamic limiting potential (*U*_L) and the intermediate binding energy in Fig. 3d and Supplementary Figs. 34, 35. The optimal active sites for the pyrrolic N, pyridinic N, armchair-edge, and pristine models are generally positioned on the right branch of the volcano (Supplementary Fig. 34), corresponding to the rate-limiting generation of OOH* (O₂ → OOH*). For these models, an increase in size primarily strengthens the adsorption of OOH*. In contrast, the active sites for the other models (e.g., graphitic N and oxygen-doped systems) are predominantly located on the left branch (Supplementary Fig. 35), where the reaction is limited by the desorption steps of either OH* (OH* → H₂O) or OOH* (OOH* → H₂O₂). Notably, within this group, larger-sized models tend to be located closer to the apex of the volcano plot, which facilitates the desorption/consumption of these rate-limiting intermediates. Overall, this thermodynamic analysis confirms that the size effect of carbon critically influences the adsorption states of key intermediates. More importantly, it reveals that the synergistic interplay between local active sites and the *sp*² domain size provides an effective strategy to adjust the reaction pathway.

Although the volcano plots provide a qualitative analysis of the activity trends for the 2e⁻ and 4e⁻ pathways, the assessment of the overall ORR selectivity is challenging, as it requires the concurrent consideration of reaction rates from both pathways. Therefore, microkinetic simulations were further performed to comprehensively evaluate the kinetic properties of both the 2e⁻ and 4e⁻ pathways⁵². Herein, for the strong-adsorption sites on the left branch of the volcano, the binding energies of OOH* (*E*_{OOH*}) and OH* (*E*_{OH*}) were used as descriptors to obtain the ORR kinetics. As shown in Fig. 3e and Supplementary Fig. 36, the reaction rate of the 4e⁻ pathway is significantly higher than that of the 2e⁻ pathway and increases with *sp*² domain size at typical potentials (0.6, 0.4, and 0.2 V vs. SHE). Notably, Fig. 3f further reveals that on small-sized carbon models, the high coverage of reaction intermediates (OOH* or OH*) passivates the active sites, leading to lower reaction rates. This passivation effect mainly arises from the multiple strengthening effects on intermediate adsorption due to “spin-charge density-edge effects” as previously reported in similar models⁵³, which can even lead to the destruction of the carbon structure, such as the C–N bond ring-opening in edge graphitic N models^{54–56}. Consequently, for these strong-adsorption models, the catalytically effective sites are primarily the larger-sized models located near the volcano apex, which proceed via the 4e⁻ pathway. Conversely, for the weak-adsorption sites on the right branch, the binding energies of OOH* (*E*_{OOH*}) and O₂* (*E*_{O₂*}) were also employed as descriptors to analyze ORR kinetics (Supplementary Fig. 37). In this case, increasing the *sp*² domain size simultaneously enhances the OOH* intermediate coverage. To further understand the underlying selectivity-regulating mechanism, an explicit solvation model based on AIMD was employed to describe the bond-breaking behavior of OOH* at the solid-liquid interface^{57,58}. Considering that calculating the free

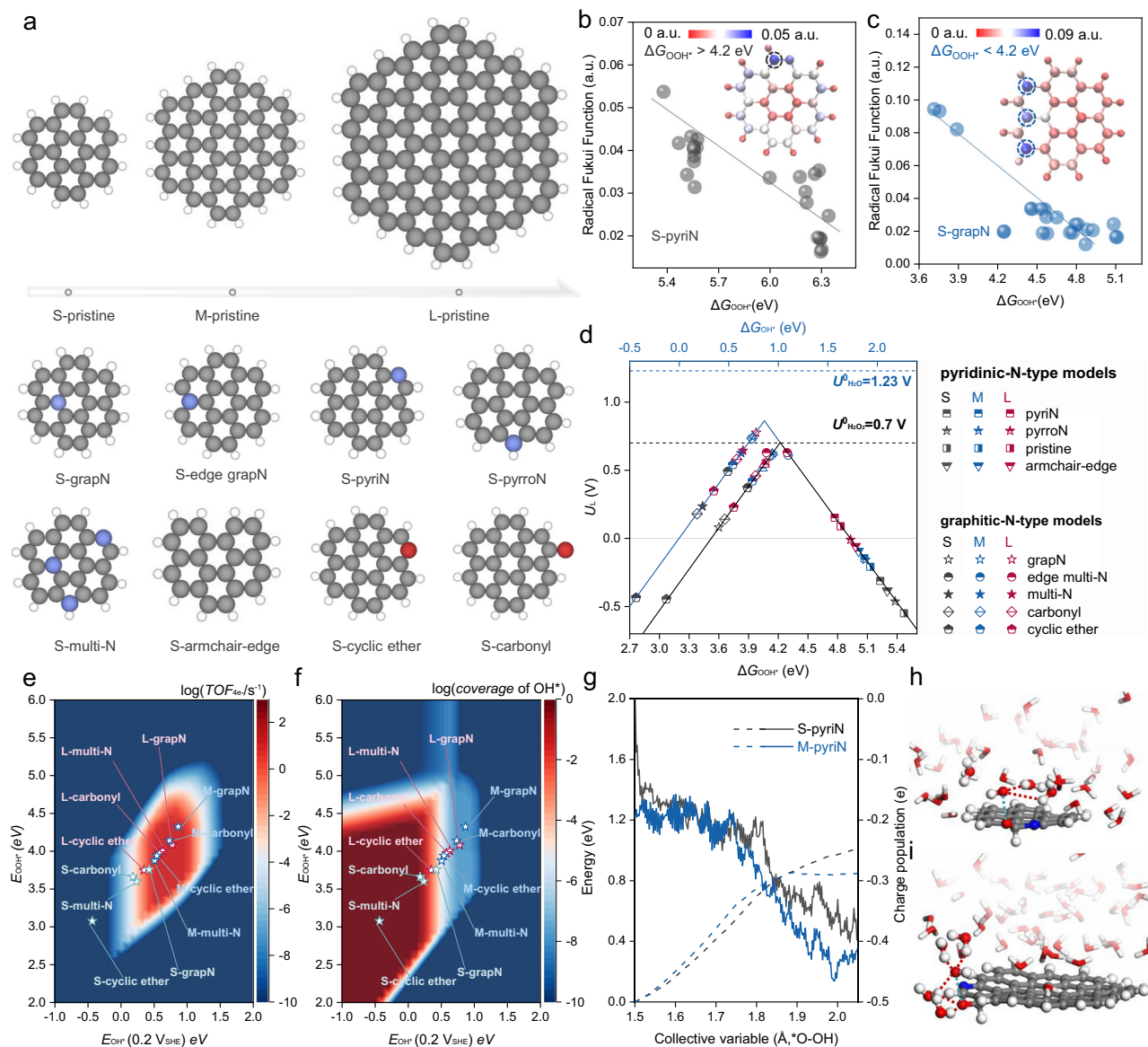


Fig. 3 | Multiscale theoretical investigation of ORR selectivity. **a** Schematic diagrams of the three doping-free carbon cluster models with varying sp^2 domain sizes and five distinct nitrogen configurations (graphitic N, pyridinic N, pyrrolic N, and multi-N doping), two oxygen configurations (epoxide and carbonyl), and an armchair-edge-terminated configuration, where the black, white, red, and blue spheres represent carbon, hydrogen, oxygen, and nitrogen atoms, respectively. Correlation between the adsorption free energy of OOH^* and the radical Fukui function for a representative pyridinic-N-type (**b**) and graphitic-N-type model (**c**).

d Calculated catalytic activity volcano plots of two-electron (solid black line) and four-electron ORR (solid blue line). **e** Microkinetically simulated turnover frequencies (TOF) on strong-adsorption models at different potentials. **f** Surface coverage of key intermediates (OH^*) on strong-adsorption models at 0.2 V vs. RHE. **g** Free energy profile (solid black line) during the O-O bond-breaking and Mulliken charge population (solid blue line) of latter O in O-OH^* for S-PyriN and M-PyriN. **h, i** Snapshots of the solvation environment around OOH^* in the final state for S-PyriN (**e**) and M-PyriN (**f**). Source data for (**b-g**) are provided as a Source Data file.

energy using AIMD is computationally expensive, especially for large-sized carbon clusters^{13,59–61}, two representative sizes from the pyridinic N models (S-pyriN and M-pyriN) in the DFT section were selected to calculate the reaction barriers for OOH^* bond dissociation (ΔG_{OOH^*}) using the slow-growth AIMD approach, as shown in Supplementary Figs. 38–42. Figure 3g illustrates the ΔG_{OOH^*} (Left axis) and the corresponding Mulliken charge population (Right axis) during the O-O bond dissociation of the OOH^* species. As the size of the carbon cluster increases, ΔG_{OOH^*} decreases from 1.01 to 0.86 eV (dashed line), indicating that active centers with a larger-sized exhibit higher selectivity toward the $4e^-$ ORR pathway, which corroborates our experimental results. Mulliken charge population analysis of the latter oxygen atoms in the O-OH^* species (solid line) further demonstrates that intermediates adsorbed on the larger-sized M-pyriN exhibit a more

negative charge, thereby promoting the breaking of the O-O bond by accepting protons from the aqueous environment. As proven in Fig. 3h, i, relative to the S-pyriN model, more hydrogen bonds (indicated by the red dashed lines) are formed between the oxygen atom in OOH^* and nearby water molecules in the M-pyriN models during the O-O bond breaking process. Overall, these multiscale calculations collectively demonstrate that larger sp^2 domain sizes intrinsically promote the $4e^-$ pathway, while the introduction of various active sites types can alter the ORR rate-limiting step, giving rise to the observed coupling effects between sp^2 carbon domains and local active sites.

In situ mechanism study

To further bridge the gap between theoretical computations and macroscopic experiments, it is crucial to identify key intermediates

(e.g., O_2^* , OOH^* , OH^*) generated at the catalyst surface during multi-proton electron transfer processes at the molecular scale. In situ Raman spectroelectrochemistry has been widely utilized to investigate the interactions between transient intermediates and the catalyst that occur during the ORR process^{9,62–65}. However, previously reported spectroscopic characterization results of carbon-based electrocatalysts during ORR process have been contentious due to the short-lived nature and low coverage of ORR intermediates^{66,67}. To address these challenges, the Shell-Isolated Nanoparticle-Enhanced Raman Spectroscopy (SHINERS) technique was employed to achieve stronger signal enhancement generated by electromagnetic fields localized at the junctions between Shell-Isolated Nanoparticles and the carbon substrate, as depicted in Fig. 4a–c^{68–71}.

Carbon soot samples used in Fig. 2 were initially employed to investigate the origin of ORR selectivity. Figure 4d–f display the in situ surface-enhanced Raman spectra of carbon soot in 0.1 M KOH solution (pH 13) saturated with O_2 , measured over a potential range from 0.96 V to -0 V vs. RHE, along with the Raman spectra of the original carbon soot at open-circuit voltage (OCV) for comparison. As observed, pristine carbon soot of various sizes exhibits distinct Raman scattering peaks corresponding to the *D*-band (1350 cm^{-1}) and *G*-band (-1590 cm^{-1}) under OCV conditions. During the ORR process, the dynamics of both *D* and *G* peaks vary with the applied potential as shown in Supplementary Fig. 43, indicating that sp^3 -hybridized carbon defect sites and sp^2 carbon sites interact strongly with adsorbed ORR intermediates or electrolytes. Interestingly, a new broad Raman band ($1000\text{--}1200\text{ cm}^{-1}$) centered at -1060 cm^{-1} appears at 0.76–0 V for three catalysts, but this signal was absent in the Ar-saturated 0.1 M KOH solution (Supplementary Fig. 44). Hence, we speculate that the new band is associated with the ORR intermediate. To further identify the intermediates, a deuterium isotopic substitution test was performed in 0.1 M KOH and KOD solutions, as illustrated in Fig. 4g. The absence of a chemical shift upon H/D isotope substitution indicates that the adsorbed oxygen-containing intermediates are not associated with hydrogen atoms. It is well-documented that the broad Raman band between 1000 and 1200 cm^{-1} appearing during oxygen electrocatalysis is commonly assigned to the O–O stretching vibration of superoxide species (O_2^-)^{72,73}. In line with these precedents, our DFT calculations indeed predict that adsorbed O_2^* exhibits a $\nu_{(O-O)}$ peak at -1000 cm^{-1} and an $^{18}O_2$ isotopic experiment revealed that this broad peak shifted from -1060 to -1000 cm^{-1} (Supplementary Fig. 45), which could be attributed to the O–O stretching vibration of an adsorbed O_2^- based on the isotopic mass formula (see Supporting Information Note). Therefore, the peak at -1060 cm^{-1} was ascribed to the O–O stretching vibration of adsorbed O_2^- (O_2^*) and the subsequent protonation step of O_2^* to form OOH^* ($O_2^* + H_2O \rightarrow OOH^* + OH^-$) should be the rate-limiting step on the pristine carbon soot in alkaline conditions. Given that the enhancement factor and spectral response of SHINERS can vary with catalyst morphology and local structure, the macroscopic isotopic kinetic experiments shown in Fig. 4h using gas diffusion electrodes in 0.1 M KOH and KOD electrolytes were also conducted to further validate the results from our in situ spectroscopic characterization. The kinetic isotope effect (*KIE*) values for the three carbon soot samples range from 0.88 to 1.37 at 0.65–0.76 V, suggesting that there is no significant kinetic isotope effect in KOD electrolyte and the ORR process does not involve proton transfer before the rate-limiting step. The corresponding Tafel slopes shown in Supplementary Fig. 46 also reveals that a slope of -60 mV dec^{-1} can be observed in both KOH and KOD electrolytes, and decreases from -75 mV dec^{-1} to 62 mV dec^{-1} as the carbon soot size increases, indicating that larger-sized carbon soot samples exhibit faster reaction kinetics, which is in agreement with the results obtained from the RRDE test in Fig. 2.

Based on the above analyses, a direct correlation between the ORR kinetics and the surface coverage of intermediates was established to experimentally validate the microkinetic predictions. To this

end, a colored contour map was constructed to display the Raman intensity at -1060 cm^{-1} as a function of the Tafel slope and potential in Fig. 4i and Supplementary Fig. 47. Given that the intensity of in situ Raman features has been demonstrated to correlate strongly with intermediate coverage, it can serve as a key experimental descriptor to validate the surface coverage trends obtained from microkinetic simulations as shown in Supplementary Fig. 37. Importantly, this map reveals that higher intensity of adsorbed O_2^* is observed at lower Tafel slopes as the sp^2 domain size increases. This provides direct experimental evidence that larger sp^2 domains accelerate ORR kinetics by enriching the surface coverage of the rate-limiting O_2^* intermediate, a trend in excellent agreement with the microkinetic simulations. By integrating molecular-scale spectroscopic results with theoretical findings from AIMD (Fig. 2g–i) and DFT located on the right branch of the volcano plot (Fig. 2d), this analysis demonstrates that the enhanced electron transfer kinetics in larger-sized sp^2 carbon domains promote the conversion of O_2 to the key adsorbed intermediate O_2^* , whose electron-rich nature facilitates its subsequent protonation and O–O bond dissociation, ultimately leading to the preferred $4e^-$ ORR pathway.

Elucidating the reaction mechanism

Above theoretical and statistical findings collectively demonstrate the non-negligible coupling influence of the intrinsic carbon domain size and local active sites. To further elucidate the coupling mechanism to guide the design of high-performance commercial ORR carbon catalysts, and to confirm the reliability of our theoretical calculations and regression model, two nitrogen-doped carbon soot samples with distinct sizes (NCS-low and NCS-top) were further prepared via in situ flame synthesis using acetonitrile as a nitrogen precursor (Fig. 5a). As directly observed from HRTEM images, NCS-top that sampled at a greater height indeed possesses significantly longer-range carbon crystallinity. Notably, despite originating from the same synthesis batch, NCS-top displays an onset potential -100 mV higher than NCS-low (Fig. 5b). Moreover, the ORR selectivity trend summarized in Fig. 5c reveals a pronounced switch in $2e^-$ selectivity, from -50% for NCS-top to -90% for NCS-low. Given the stark differences in ORR performance between the newly prepared NCS-low and NCS-top samples, their physicochemical properties were subsequently characterized via XPS and Raman spectroscopy (Supplementary Figs. 48, 49 and Supplementary Table 3). In order to quantitatively dissect the contributions of various structural factors to this performance gap, an *F*-test was conducted on the key variables from our established regression model (Supplementary Fig. 50). The analysis reaffirms that the sp^2 domain size (represented by $\sqrt{I_D/I_G}$) is the most statistically significant variable ($F=64$). Remarkably, the experimental $2e^-$ ORR selectivity of the new NCS samples aligns perfectly with the trend line predicted by our regression model (Fig. 5d), thereby providing robust validation of the model's predictive efficacy. However, unlike the nitrogen-free carbon soot, further *KIE* studies as exhibited in Fig. 5e indicate that the larger-sized NCS-top exhibits a significantly more pronounced isotope effect, implying that the cleavage of the O–H bond in water molecules is likely involved before the rate-determining step of ORR in these nitrogen-doped systems. Similar phenomena have also been observed in our nitrogen-doped GQDs catalysts, as shown in Supplementary Fig. 51, where the *KIE* values of GQDs increase from -6 to 15 with increasing size. This provides substantial evidence that the coupling of nitrogen dopants and carbon domain size alters the ORR reaction pathway.

To investigate this coupling mechanism at the molecular level, in situ surface-enhanced Raman spectroscopy was performed on NCS-top and NCS-low in O_2 -saturated 0.1 M KOH at various potentials. As shown in Fig. 5f, g, the Raman spectra exhibit a distinct Raman band at 1060 cm^{-1} during the ORR process, which was attributed to O–O vibrations in adsorbed O_2^* . A quantitative comparison of this

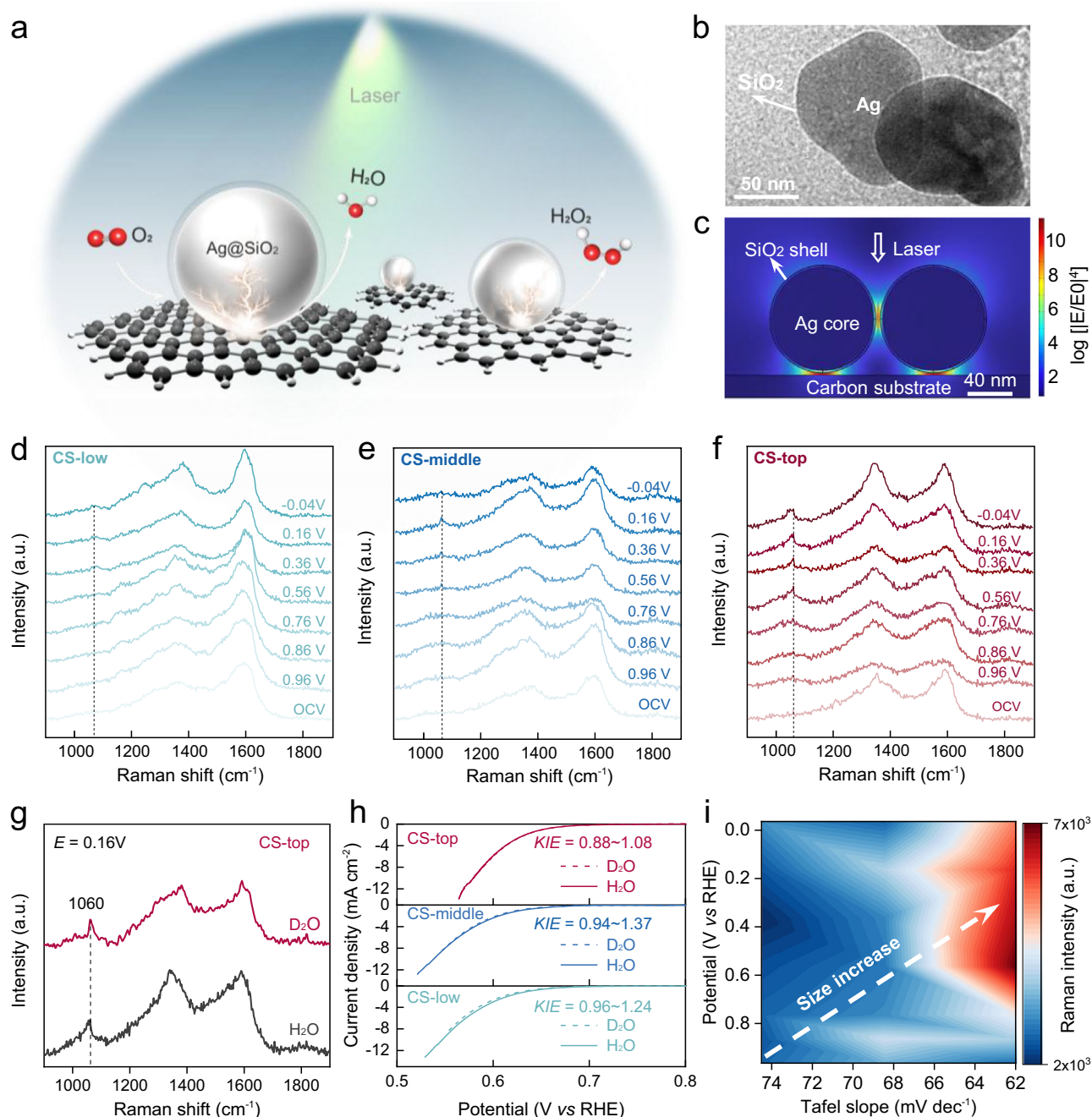


Fig. 4 | In situ Raman spectroscopy and kinetic analysis of ORR on carbon soot.

a Schematic illustration of the shell-isolated nanoparticles (Ag@SiO_2) on the surface of carbon-based catalysts with different sizes and the mechanism of the ORR process revealed by the SHINERS method, where the black, white, and red spheres represent carbon, hydrogen, and oxygen atoms, respectively. **b** TEM image of Ag@SiO_2 . **c** Electromagnetic field distribution of Ag@SiO_2 on the glassy carbon substrate, where E and E_0 denote the localized electric field and the incident electric field. In situ surface-enhanced Raman spectra of the ORR system at the surface of

CS-low (**d**), CS-middle (**e**), and CS-top (**f**) in a 0.1 M KOH solution saturated with O_2 . **g** In situ surface-enhanced Raman spectra of CS-top catalyst in O_2 -saturated 0.1 M KOH and 0.1 M KOD at 0.16 V vs. RHE. **h** LSV curves of CS-low, CS-middle and CS-top under gas diffusion electrode setup in 0.1 M KOH and 0.1 M KOD with iR-compensation. **i** Colored contour map of Raman intensity at 1060 cm^{-1} as a function of Tafel slope of CS-low, CS-middle and CS-top and potential in O_2 -saturated 0.1 M KOH. Source data for (**d**–**i**) are provided as a Source Data file.

potential-dependent Raman intensity of the O_2^* intermediate is presented in Fig. 5h, which shows that the G-peak-normalized Raman intensity of O_2^* gradually increases for both NCS-top and NCS-low as the potential decreases to -0.4 V (vs. RHE) and NCS-top consistently exhibits stronger vibrational signals. This indicates that the synergistic interplay between a larger sp^2 domain size and the statistically significant N-doping configurations ($\sqrt{I_D/I_G} \times (\text{PyriN} + \text{PyrroN})$ and $(\text{PyriN} + \text{PyrroN})$ in Supplementary Fig. 50) collectively enhances the surface coverage of this key intermediate. Interestingly, NCS-top

catalyst showed decreased intensities of O_2^* bands at potentials below 0.4 V , likely attributable to the faster consumption of O_2^* due to a switch in the ORR rate-limiting step, as corroborated by the pronounced isotope effect observed for NCS-top in D_2O . Under these conditions, Fig. 5g indeed reveals an additional peak for NCS-top located around 1535 cm^{-1} in addition to the peak at 1060 cm^{-1} . For the identification of this new species, H/D isotopic substitution measurements confirm this peak undergoes a redshift to 1510 cm^{-1} (Supplementary Fig. 52), implying that the peak at 1530 cm^{-1} is associated with

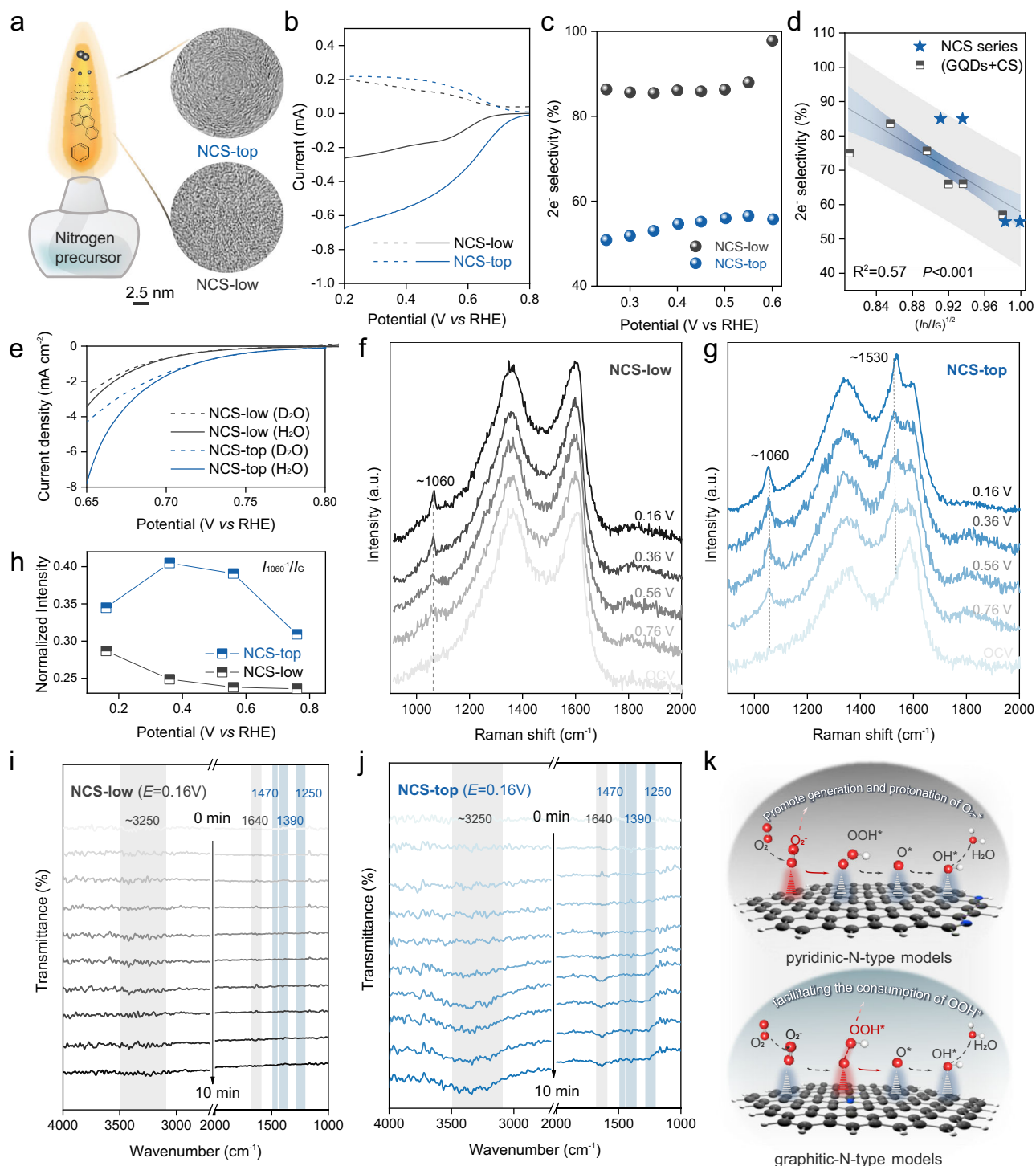


Fig. 5 | Experimental validation and mechanistic investigation of the synergistic effect between sp^2 domain size and nitrogen doping. **a** Schematic of the in situ flame synthesis setup for preparing nitrogen-doped carbon soot (NCS) samples and representative HRTEM images of NCS-low and NCS-top. Scale bars, 2.5 nm. **b** RRDE polarization curves (solid lines) and H_2O_2 detection currents (dashed lines) in 0.1 M KOH at 1600 r.p.m without iR-compensation. **c** Calculated $2e^-$ ORR selectivity for NCS-low and NCS-top based on RRDE tests. **d** Validation of the PLSR model. **e** LSV curves for NCS-low and NCS-top measured with a gas

diffusion electrode (GDE) setup in 0.1 M KOH and 0.1 M KOD with iR-compensation. **f, g** In situ surface enhanced Raman spectra of the ORR system in a 0.1 M KOH solution saturated with O_2 . **h** Potential-dependent, G-peak-normalized Raman intensities of the O_2^* intermediates for NCS-low and NCS-top. Time-dependent in situ ATR-FTIR spectra of **(i)** NCS-low and **(j)** NCS-top under ORR conditions ($E = 0.16$ V). **k** Schematic illustration of the proposed synergistic mechanism, where the black, white, blue, and red spheres represent carbon, hydrogen, nitrogen, and oxygen atoms, respectively. Source data for **(b–j)** are provided as a Source Data file.

an H-containing species. Quantitative calculations based on chemical shift further indicate that this peak can be attributed to the O-H vibration in the OOH^* intermediate (Supporting Information Note). In line with our DFT calculations and microkinetic simulations (Fig. 3d, e),

the emergence of this OOH^* intermediate can be attributed to the strong adsorption of rate-limiting intermediates on models from the left branch of the volcano plot (e.g., graphitic N and multi-N doping), where a larger domain size enhances the reaction rate, leading to a

higher OOH* coverage. Furthermore, it can also be clearly observed that the normalized intensity of OOH* on the NCS-top surface (Fig. 5g) is significantly enhanced as the potential becomes more negative, a trend also validated by microkinetic simulations at various potentials, as illustrated in Supplementary Fig. 53. To address the potential limitations of SHINERS as a local probe and further provide bulk-averaged spectroscopic evidence, we also performed in situ Attenuated Total Reflection Fourier Transform Infrared (ATR-FTIR) spectroscopy on both NCS-low and NCS-top catalysts (Supplementary Fig. 54). As presented in Fig. 5i, j, the time-dependent ATR-FTIR spectra reveal distinct differences between the two catalysts under ORR conditions ($E = 0.16\text{ V}$ vs. RHE). For the NCS-top sample, three characteristic absorption bands for oxygen-related species can be identified, where the bands at -1470 cm^{-1} , 1390 cm^{-1} and 1250 cm^{-1} are attributed to the adsorbed molecular oxygen (O_2^*), hydroperoxide species (HOOH^*), and adsorbed superoxide (OOH^*), respectively^{74,75}. Notably, the intensity of the OOH* band at -1250 cm^{-1} significantly increases over time, indicating a substantial accumulation and higher coverage of this key intermediate on the catalyst surface. In contrast, these characteristic bands, particularly the prominent OOH* signal, are remarkably absent or significantly weaker on the NCS-low sample under identical experimental conditions. In summary, these observations via bulk-averaged in situ FTIR confirm the presence of the OOH* intermediate on NCS-top and strongly support the results from SHINERS analyses and microkinetic simulations.

Based on the above statistical validation, in situ spectroscopy, and electrochemical H/D isotope substitution tests, the synergistic interaction between the size effect and local active sites is summarized in Fig. 5k. It is well-established that the widely reported carbon-based active site engineering significantly influences the ORR rate-limiting type (from O_2^* to OOH*). Building on this, the sp^2 domain size further modulates the influence of these active sites on reaction intermediates within the carbon matrix, either by promoting the conversion of O_2^* to OOH* and subsequent O-O bond dissociation (corresponding to the right branch of the volcano plot) or by facilitating the consumption of OOH* to enhance the reaction rate (corresponding to the left branch of the volcano plot), all of which enable the ORR pathway to switch from $2e^-$ to $4e^-$.

Origin of electronic structure

To further elucidate the electronic origins of the observed size effect and its synergy with heteroatoms and defects on ORR kinetics, density of states (DOS) calculations were performed for all the models to correlate adsorbate binding strength with p -band characteristics, which reflect the overall degree of electron delocalization in the π -conjugated system. Essentially, analogous to the conventional d -band center descriptor for metallic catalysts, the adsorbate-surface interaction on carbon catalysts can be described by the p -band center (ϵ_p)^{76,77}. In this regard, the Newns-Anderson-Grimley model provides the common physical basis for both the p - and d -band descriptors⁷⁸. This model frames chemisorption as a hybridization event between the discrete orbitals of the adsorbate and the continuous electronic bands of the catalyst surface, wherein the resulting energies and fillings of the newly formed states ultimately determine the bond strength. As illustrated in Fig. 6a, the broad p -band of carbon catalysts leads to a broadening of the states of the OOH* intermediate into resonances, where a higher ϵ_p weakens the adsorption by pushing the resonance closer to the Fermi level. Conversely, on a metal surface (Fig. 6b), the narrow d -band causes a splitting into bonding and anti-bonding orbitals, with the filling of the latter determining the binding strength.

The band-structure analysis presented here provides a unified framework for understanding adsorbate binding behavior across the volcano plot. Focusing first on the right-leg side of the volcano plot (weak-binding region), the partial density of states (PDOS) in Supplementary Fig. 55 reveals that the ϵ_p shifts to lower energies with

increasing carbon domain size. This downward shift of the electronic descriptor directly translates into predictable adsorption energetics. Figure 6c illustrates that the lower ϵ_p of larger-sized carbon domains stabilizes the p -adsorbate resonance state of the OOH* intermediate (particularly its $2\pi^*$ anti-bonding orbital) at a lower energy (blue arrows), which in turn facilitates stronger OOH* adsorption. The validity of this principle is quantitatively confirmed in Fig. 6d, which provides a direct comparison with conventional DFT-based adsorption energy trends by showing that the adsorption of OOH* becomes stronger as the ϵ_p shifts to lower energies in larger-sized carbon domains. This finding is also consistent with results for other pyridinic-N type models (Supplementary Fig. 56). In stark contrast, the strong-binding sites on the left side of the volcano plot are predominantly located at carbon edges and exhibit significant spin polarization (Supplementary Figs. 30–33). Consequently, the standard Newns-Anderson-Grimley model is unable to account for spin-dependent interactions that result in non-linear deviations from the simple band-center model, particularly for systems with localized electronic states such as p -states at carbon edges, due to its inherent non-magnetic characteristics^{79,80}. Indeed, this spin polarization complicates the direct application of an averaged p -band center model, as the spin-up and spin-down sub-bands form two distinct sets of bonding and anti-bonding orbitals with the adsorbate⁸¹. To address the role of spin polarization and provide a direct comparison with conventional DFT-based adsorption energy trends for these strong-binding sites, the PDOS of the active sites in the graphitic-N models before and after OOH* adsorption was also analyzed (Fig. 6e). The results show that the p -band centers of spin-up and spin-down states become closer due to hybridization with the OOH* intermediate. Here, the p -band center gaps (Δp) of S-grapN, M-grapN, L-grapN are 1.45, 0.76, and 0.67 eV, respectively, meaning the Δp is related to the OOH* adsorption strength⁸². Figure 6f quantitatively validates this descriptor by plotting it against the DFT-calculated OOH* adsorption strength, which simultaneously demonstrates that the larger Δp in smaller sp^2 domains leads to an over-binding of the intermediate that hinders its subsequent desorption. This trend, further supported by our microkinetic simulations and observed in other strong-binding models on the left side of the volcano plot (Supplementary Fig. 57), confirms that Δp serves as a predictive descriptor for adsorption energetics on spin-polarized carbon sites. Taken together, this comprehensive p -band analysis not only shows excellent agreement with our experimental and computational findings but also establishes a definitive correlation between the ORR selectivity and the p -band theory.

Discussion

Taken together, the underlying coupling mechanism by which the size of sp^2 carbon domains and local active sites switch ORR selectivity between $2e^-$ and $4e^-$ pathways is revealed through the controllable synthesis of model carbon catalysts. In situ spectroscopy and multi-scale theoretical computations mutually corroborate that while local active sites determine the rate-limiting intermediate type, increasing sp^2 domain size facilitates the ORR mechanism switch from $2e^-$ to $4e^-$ pathway by modulating the formation, bond-breaking, and desorption behaviors of rate-limiting intermediates (O_2^* , OOH* and OH*), the nature of which is determined by the local active sites. To further demonstrate the synergistic effect, a nitrogen-doped carbon soot catalyst with significantly different carbon domain sizes is shown to induce a profound change in the ORR reaction pathway and $2e^-$ selectivity from $\sim 50\%$ to over 90% , offering direct experimental evidence of the coupling effect between sp^2 carbon domain size and active sites. Ultimately, the revealed dual coupling mechanisms for switching ORR selectivity on carbon catalysts in our work can also be perfectly integrated with p -band theory. Our work not only provides an intelligent strategy to regulate ORR selectivity by tailoring size of sp^2 domains in carbon-based electrocatalysts but can also be further

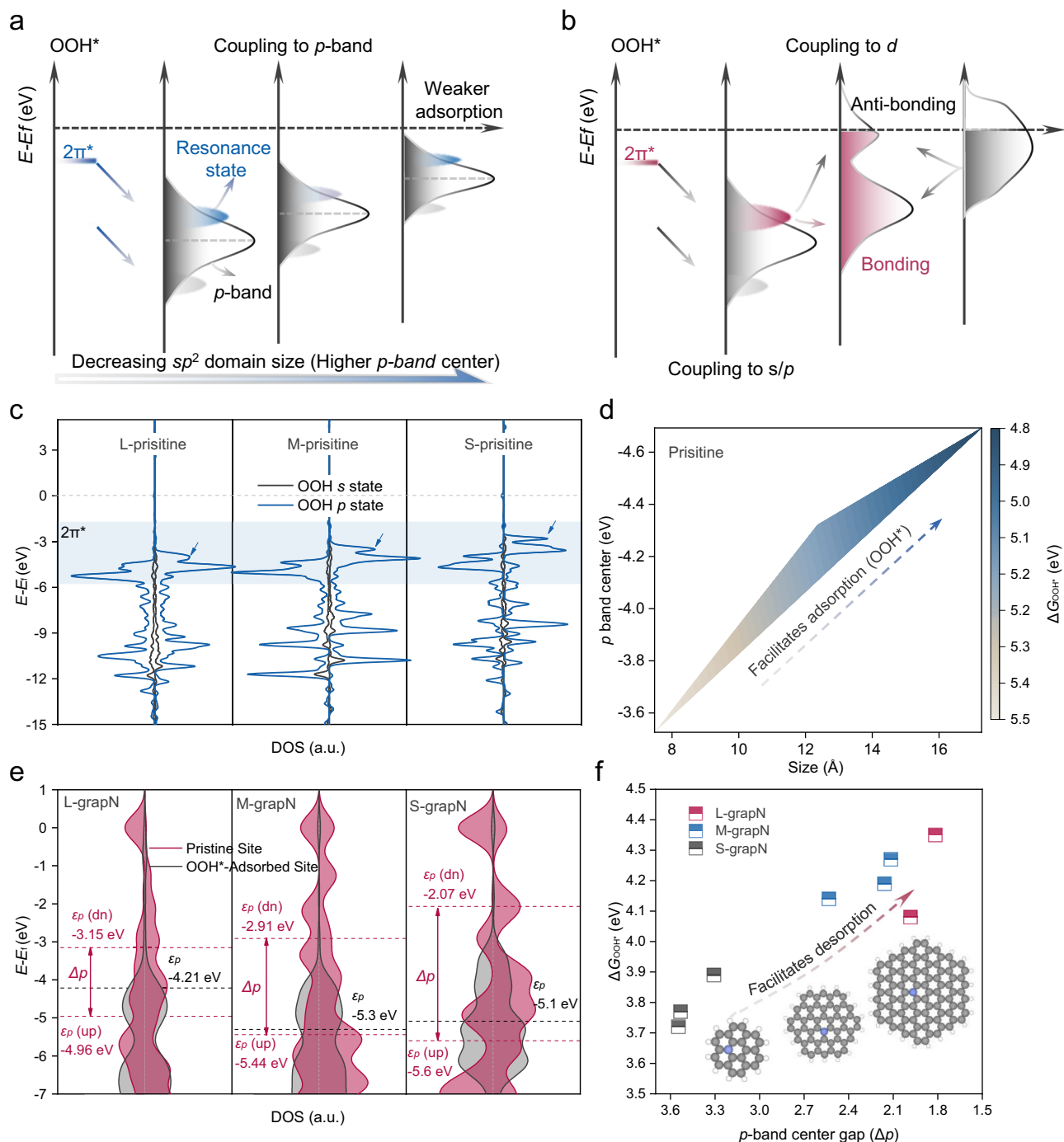


Fig. 6 | Electronic origin of the ORR selectivity from band theory. Schematic comparison of adsorbate-surface interactions for **a** carbon catalysts governed by the p -band model and **b** metallic catalysts governed by the d -band model.

c Correlation between the p -band center (ϵ_p) of the active site and the sp^2 domain size for pristine models. **d** Colored contour map of adsorption energy of OOH^* (ΔG_{OOH^*}) as a function of size and p -band center. **e** Spin-polarized PDOS of the

active site in the GrapN models before (black) and after (red) OOH^* adsorption.

f Correlation between the spin-polarization-induced p -band center gap (Δp) and ΔG_{OOH^*} for graphitic-N models. The inset schematics illustrate the atomic structures, where the black, white, and blue spheres represent carbon, hydrogen, and nitrogen atoms, respectively. Source data for Figure (c-f) are provided as a Source Data file.

extended to other carbon-catalyzed electrochemistry, such as CO_2 or N_2 electrochemical reduction reactions.

Methods

Materials

All chemicals and materials were of analytical grade or higher and were used as received without further purification. Potassium hydroxide (KOH, $\geq 90\%$ purity, flakes) was purchased from Sigma-Aldrich and

graphene was obtained from XFNANO. Hydrogen peroxide (H_2O_2 , 30 wt% in H_2O), ammonia solution ($\text{NH}_3\cdot\text{H}_2\text{O}$, $\geq 28\%$), potassium deuteroxide solution (KOD, 30 wt% in D_2O), paraffin wax (melting point: 58–60 °C) and acetonitrile (CH_3CN , 99.8%) were procured from Aladdin. Chloroauric acid tetrahydrate (HAuCl_4), ascorbic acid, sodium citrate, sodium silicate, and sodium borohydride (NaBH_4) were purchased from Sinopharm Chemical Reagent Co. Ltd. (3-aminopropyl) trimethoxysilane (ATPMS) and Anhydrous silver perchlorate (AgClO_4 ,

99%) were purchased from Alfa Aesar. Hydrophobic carbon cloth with a microporous layer (W1S1010) was supplied by CeTech. All aqueous solutions, including the 0.1 M KOH electrolyte, were prepared using ultrapure deionized water (18.2 M Ω -cm at 25 °C) from a Millipore Milli-Q purification system.

Catalyst synthesis

Synthesis of Graphene quantum dots with various sp^2 domain sizes.

GQDs were synthesized by oxidizing 200 mg of graphene oxide (GO) sheets in a concentrated solution containing 25 mL of 30 wt% H₂O₂ and 20 mL of NH₃·H₂O ($\geq 28\%$) at -90 °C (Supplementary Fig. 2). After heating for 1–2 h, the initially dark brown GO solution transformed into a yellow-green solution, and the mixture was subsequently filtered through a 100 nm nanoporous membrane to remove the larger GO sheets. Following the freeze-drying process, impurity-free GQD powders were obtained due to the evaporation of H₂O₂ and NH₃·H₂O. To obtain graphene quantum dots (GQDs) with varying sizes, the GQD powders were dissolved in deionized water and separated utilizing multiple dialysis bags with molecular weight cutoffs between 500 and 50,000 Da as per established protocols in previous research studies (Supplementary Figs. 3, 4)²¹.

Synthesis of carbon soot with various sp^2 domain sizes. Carbon soot was prepared during incomplete combustion of a candle flame or acetonitrile. During the incomplete combustion of candle flame, polycyclic aromatic hydrocarbons (PAHs) and soot formed at different heights inside the flame are deposited onto a glass substrate, and model catalysts of different sizes are obtained by collecting carbon soot at different heights on the glass substrate.

Physical characterizations

X-ray photoelectron spectra (XPS) analyses were conducted on a Thermo ESCALAB 250Xi System using Al K α X-ray. Survey spectra were conducted with a 100 eV pass energy and 1 eV step size. The N 1s, O 1s and C 1s spectra were analyzed with a 20 eV pass energy and 0.05 eV step size. Moreover, all the binding energies were calibrated using the C 1s level at 284.7 eV. The Raman spectra (Raman) were collected by a Raman spectrometer (Beijing, Zolix Instruments Co., Ltd.) with a 50 \times lens and an excitation wavelength of 532 nm. The transmission electron microscope (FEI Tecnai F20) was used to collect the TEM images.

Electrochemical measurements

In accordance with our previous reports⁶⁵, a drop-cast method was employed to prepare the ink for working electrodes (RRDE and GDE) and is briefly outlined as follows. 5 mg of catalyst powders were dispersed into a mixture of Nafion (30 μ L, 5 wt%) and ethanol (1 mL), followed by ultrasonication for 30 min to achieve a highly homogeneous dispersion of catalyst powders. Subsequently, the prepared catalyst ink was carefully drop-cast onto the glassy carbon disk (4 μ L, electrode area: 0.246 cm²) or gas diffusion substrate (110 μ L, electrode area: 1 cm²). This procedure resulted in a final catalyst loading of -0.08 mg cm⁻² for the RRDE and 0.53 mg cm⁻² for the GDE. All electrodes were then dried under ambient conditions.

The RRDE performances of carbon catalysts at the electrode rotation speed of 1600 r.p.m. were evaluated by employing a computer-controlled BioLogic-VMP3 workstation in a standard single-compartment glass cell using a three-electrode system. Mainly, Linear sweep voltammetry (LSV) was performed at a scan rate of 10 mV s⁻¹ in an O₂-saturated electrolyte from 1.1 V (vs. RHE) to 0.2 V (vs. RHE). The measurement was repeated independently three times, and the stable data were chosen for presentation. Ring electrode potential was set at 1.2 V (vs. RHE) to detect the amount of H₂O₂ produced. A high-purity graphite rod was used as the counter electrode and an Ag/AgCl (saturated KCl) served as the reference electrode. The electrolyte had a

specific volume (100 mL) of 0.1 M KOH (pH = 13 \pm 0.2). To ensure consistency, the 0.1 M KOH electrolyte was freshly prepared before experiments.

All potentials measured against Ag/AgCl were converted to the RHE scale using⁸³:

$$E_{vs. RHE} = E_{vs. AgCl} + 0.197V + 0.059 \times pH \quad (1)$$

Unless otherwise specified, all electrochemical data presented in this study were reported without iR correction. The 2e⁻ selectivity (molar selectivity of H₂O₂: fraction of O₂ used for producing H₂O₂) can be calculated based on the ring current density (J_R) and disk current density (J_D)^{7,84}

$$H_2O_2(\%) = 200 \times \frac{J_{H_2O_2}}{J_D + J_{H_2O_2}} \quad (2)$$

$$J_{H_2O_2} = \frac{J_R}{N} \quad (3)$$

Where N is the collection efficiency (0.339 after calibration). Using this method, the H₂O₂ selectivity was calculated as a function of the applied potential across the entire LSV scan range.

The Tafel plots were generated according to the following Tafel equation^{5,85}:

$$E = a + b \log(j_k) \quad (4)$$

Where E , a , and b represent the applied potential, constant related to the exchange current, and Tafel slope, respectively. The kinetic current (j_k) was extracted by correcting the mass-transport effect according to the following relation:

$$\frac{1}{j} = \frac{1}{j_k} + \frac{1}{j_1} \quad (5)$$

Where j_1 is the diffusion-limited current, which was selected as the highest current measured in the entire potential range.

To minimize mass-transport limitations, H/D isotope substitution experiments were conducted in a gas diffusion electrode (GDE) configuration. For these measurements, manual iR correction was applied to ensure accurate kinetic analysis, as explicitly noted in the corresponding figure caption. The electrochemical cell was identical to the RRDE setup, except for the introduction of a proton exchange membrane (Nafion™ N117, 183 μ m thick, 2 cm diameter) to separate the cathode and anode. The membrane was pre-treated before use by boiling at 80 °C for 1 h each in a sequence of 5% H₂O₂, deionized water, 0.5 M H₂SO₄, and finally deionized water. Electrochemical impedance spectroscopy (EIS) measurements were performed over a frequency range of 100 kHz to 0.1 Hz with a 10 mV amplitude under various potentials. The resulting data were analyzed using the distribution of relaxation times (DRT) method. (A detailed impedance analysis is provided in the Supplementary Methods). Electrochemical active surface area (ECSA) was estimated by measuring the electrochemical double-layer capacitance (Cdl). Cyclic voltammetry (CV) curves were recorded in a non-Faradaic potential window at various scan rates (10–100 mV s⁻¹) and the Cdl was determined by plotting the current density difference ($\Delta j = j_a - j_c$) at the center of the potential window against the scan rate.

In situ measurements

Preparation of shell-isolated Ag nanostructures. The spherical Ag NPs were synthesized through a seed growth method in which Au NPs served as seeds: 50 ml of 0.02% HAuCl₄ aqueous solution was

heated to boiling. 1.5 ml of 1 wt% sodium citrate solution was quickly added while stirring, and the solution was boiled for 30 min. Subsequently, the solution was cooled to room temperature for later use. The diluted Au seeds were then mixed with sodium citrate and ascorbic acid, and AgClO_4 was added to the mixture. The concentrations of sodium citrate, ascorbic acid, and AgClO_4 were 0.55, 0.55, and 0.69 mM, respectively. To synthesize the shell-isolated Ag NPs, 11 ml of the as-prepared Ag nanoparticle sol was stirred for uniform mixing. NaBH_4 , APTMS, and sodium silicate were then added to the Ag sol while stirring. The quantities of NaBH_4 , APTMS, and sodium silicate in the mixture were 5 mM, 0.26 mM, and 0.069%, respectively. Throughout the preparation process, the pH value of the growth solution was adjusted to ~ 9.5 using H_2SO_4 . The growth solution was heated at 90 °C and stirred for 60 min. Subsequently, the bath temperature was reduced to 60 °C, and stirring continued for an additional 30 min.

In situ Raman measurements. In situ Raman measurements were performed using a confocal Raman spectrometer equipped with a $50\times/0.8$ NA objective. A homemade 3D-printed electrochemical cell was assembled, incorporating an Ag/AgCl reference electrode, a graphite rod counter electrode, and glassy carbon (GC, diameter 0.2 cm) working electrodes (Supplementary Fig. 43a). Prior to the Raman test, GC working electrodes were polished with Al_2O_3 powder slurries to achieve a smooth surface and then washed with ultrapure Milli-Q water (18.2 M Ω cm). During the Raman measurements, a 532 nm laser (20–25 mW) focused on the GC electrode decorated with $\text{Ag}@/\text{SiO}_2$ and carbon-based catalyst. The Raman scattered photons were dispersed using the 1800 g/mm grating, and the acquisition time was set at 5 s under controlled chronoamperometry at the potential of interest. Prior to analysis, the resulting in situ spectra were baseline-corrected to remove the fluorescence background. To minimize the weakening effect of the solution layer (0.1 M KOH) on the Raman signal, the distance between the sapphire window and the working electrode surface was maintained at less than 0.5 mm.

Data availability

The data supporting the findings of this study are available within the paper and its Supplementary Information. Source data are provided with this paper.

References

- Gong, K. et al. Nitrogen-doped carbon nanotube arrays with high electrocatalytic activity for oxygen reduction. *Science* **323**, 760–764 (2009).
- Hu, C. et al. Carbon-based metal-free electrocatalysts: from oxygen reduction to multifunctional electrocatalysis. *Chem. Soc. Rev.* **50**, 11785–11843 (2021).
- Guo, D. et al. Active sites of nitrogen-doped carbon materials for oxygen reduction reaction clarified using model catalysts. *Science* **351**, 361–365 (2016).
- Jia, Y. et al. Identification of active sites for acidic oxygen reduction on carbon catalysts with and without nitrogen doping. *Nat. Catal.* **2**, 688–695 (2019).
- Sa, Y. J. et al. Active edge-site-rich carbon nanocatalysts with enhanced electron transfer for efficient electrochemical hydrogen peroxide production. *Angew. Chem. Int. Ed.* **58**, 1100–1105 (2019).
- Chen, S. et al. Designing boron nitride islands in carbon materials for efficient electrochemical synthesis of hydrogen peroxide. *J. Am. Chem. Soc.* **140**, 7851–7859 (2018).
- Xia, Y. et al. Highly active and selective oxygen reduction to H_2O_2 on boron-doped carbon for high production rates. *Nat. Commun.* **12**, 4225 (2021).
- Lu, Z. et al. High-efficiency oxygen reduction to hydrogen peroxide catalysed by oxidized carbon materials. *Nat. Catal.* **1**, 156–162 (2018).
- Kim, H. W. et al. Efficient hydrogen peroxide generation using reduced graphene oxide-based oxygen reduction electrocatalysts. *Nat. Catal.* **1**, 282–290 (2018).
- Han, G.-F. et al. Building and identifying highly active oxygenated groups in carbon materials for oxygen reduction to H_2O_2 . *Nat. Commun.* **11**, 2209 (2020).
- Fellinger, T.-P. et al. Mesoporous nitrogen-doped carbon for the electrocatalytic synthesis of hydrogen peroxide. *J. Am. Chem. Soc.* **134**, 4072–4075 (2012).
- Tian, Q. et al. Mesoporous carbon spheres with programmable interiors as efficient nanoreactors for H_2O_2 electrosynthesis. *Nat. Commun.* **15**, 983 (2024).
- Zhao, X. et al. Origin of selective production of hydrogen peroxide by electrochemical oxygen reduction. *J. Am. Chem. Soc.* **143**, 9423–9428 (2021).
- Fernandez-Escamilla, H. N. et al. Understanding the selectivity of the oxygen reduction reaction at the atomistic level on nitrogen-doped graphitic carbon materials. *Adv. Energy Mater.* **11**, 2002459 (2021).
- Cui, P. et al. Carbon-based electrocatalysts for acidic oxygen reduction reaction. *Angew. Chem. Int. Ed.* **62**, e202218269 (2023).
- Paul, R. et al. Charge transfer of carbon nanomaterials for efficient metal-free electrocatalysis. *Interdiscip. Mater.* **1**, 28–50 (2022).
- Zhai, Q. et al. Carbon-based metal-free electrocatalysts: past, present, and future. *Acc. Mater. Res.* **2**, 1239–1250 (2021).
- Li, Q. et al. Nitrogen-doped colloidal graphene quantum dots and their size-dependent electrocatalytic activity for the oxygen reduction reaction. *J. Am. Chem. Soc.* **134**, 18932–18935 (2012).
- Choi, C. H. et al. Long-range electron transfer over graphene-based catalyst for high-performing oxygen reduction reactions: importance of size, N-doping, and metallic impurities. *J. Am. Chem. Soc.* **136**, 9070–9077 (2014).
- Kim, H. W. et al. Mechanisms of two-electron and four-electron electrochemical oxygen reduction reactions at nitrogen-doped reduced graphene oxide. *ACS Catal.* **10**, 852–863 (2020).
- Kim, S. et al. Anomalous behaviors of visible luminescence from graphene quantum dots: interplay between size and shape. *ACS Nano* **6**, 8203–8208 (2012).
- Shiraishi, Y. et al. Photocatalytic hydrogen peroxide splitting on metal-free powders assisted by phosphoric acid as a stabilizer. *Nat. Commun.* **11**, 3386 (2020).
- Geng, B. et al. Near-infrared phosphorescent carbon dots for sonodynamic precision tumor therapy. *Nat. Commun.* **13**, 5735 (2022).
- Liu, J. et al. Metal-free efficient photocatalyst for stable visible water splitting via a two-electron pathway. *Science* **347**, 970–974 (2015).
- Yu, L. et al. Disclosing the natures of carbon edges with gradient nanocarbons for electrochemical hydrogen peroxide production. *Matter* **5**, 1909–1923 (2022).
- Liu, C. et al. Flame-formed carbon nanoparticles exhibit quantum dot behaviors. *Proc. Natl. Acad. Sci. USA* **116**, 12692–12697 (2019).
- Ferrari, A. C. Raman spectroscopy of graphene and graphite: disorder, electron-phonon coupling, doping and nonadiabatic effects. *Solid State Commun.* **143**, 47–57 (2007).
- Liu, R. et al. Nitrogen-doped ordered mesoporous graphitic arrays with high electrocatalytic activity for oxygen reduction. *Angew. Chem. Int. Ed.* **49**, 2565–2569 (2010).
- Li, L. et al. Tailoring selectivity of electrochemical hydrogen peroxide generation by tunable pyrrolic-nitrogen-carbon. *Adv. Energy Mater.* **10**, 2000789 (2020).
- Wang, N. et al. Graphitic nitrogen is responsible for oxygen electroreduction on nitrogen-doped carbons in alkaline electrolytes: insights from activity attenuation studies and theoretical calculations. *ACS Catal.* **8**, 6827–6836 (2018).

31. Wang, T. et al. Identifying the active site of N-doped graphene for oxygen reduction by selective chemical modification. *ACS Energy Lett.* **3**, 986–991 (2018).
32. Geng, D. et al. High oxygen-reduction activity and durability of nitrogen-doped graphene. *Energy Environ. Sci.* **4**, 760–764 (2011).
33. Lai, L. et al. Exploration of the active center structure of nitrogen-doped graphene-based catalysts for oxygen reduction reaction. *Energy Environ. Sci.* **5**, 7936–7942 (2012).
34. Kumar, K. Partial least square (PLS) analysis: most favorite tool in chemometrics to build a calibration model. *Resonance* **26**, 429–442 (2021).
35. Liu, C. et al. Partial least squares regression and principal component analysis: similarity and differences between two popular variable reduction approaches. *Gen. Psychiatry* **35**, e100662 (2022).
36. Chang, D. et al. Soot morphology and nanostructure differences between Chinese aviation kerosene and algae-based aviation bio-fuel in free jet laminar diffusion flames. *ACS Omega* **7**, 11560–11569 (2022).
37. Botero, M. L. et al. Internal structure of soot particles in a diffusion flame. *Carbon* **141**, 635–642 (2019).
38. Botero, M. L. et al. HRTEM evaluation of soot particles produced by the non-premixed combustion of liquid fuels. *Carbon* **96**, 459–473 (2016).
39. Vitiello, G. et al. Role of radicals in carbon clustering and soot inception: a combined EPR and Raman spectroscopic study. *Combust. Flame* **205**, 286–294 (2019).
40. Commodo, M. et al. Physicochemical evolution of nascent soot particles in a laminar premixed flame: from nucleation to early growth. *Combust. Flame* **162**, 3854–3863 (2015).
41. Zhang, Q. et al. Direct insights into the role of epoxy groups on cobalt sites for acidic H₂O₂ production. *Nat. Commun.* **11**, 4181 (2020).
42. Lee, S. W. et al. High-power lithium batteries from functionalized carbon-nanotube electrodes. *Nat. Nanotechnol.* **5**, 531–537 (2010).
43. Wu, Q. et al. Ultra-dense carbon defects as highly active sites for oxygen reduction catalysis. *Chem* **8**, 2715–2733 (2022).
44. Jia, Y. et al. Defect electrocatalytic mechanism: concept, topological structure and perspective. *Mater. Chem. Front.* **2**, 1250–1268 (2018).
45. Olson, T. S. et al. Bifunctional oxygen reduction reaction mechanism on non-platinum catalysts derived from pyrolyzed porphyrins. *J. Electrochem. Soc.* **157**, B54 (2009).
46. Wu, Y. et al. Rotating ring-disk electrode theory and method to correct quasi-four-electron oxygen reduction over Fe/N/C and N/C cathode catalysts. *Curr. Opin. Electrochem.* **25**, 100633 (2021).
47. Tan, X. et al. Understanding the high activity of mildly reduced graphene oxide electrocatalysts in oxygen reduction to hydrogen peroxide. *Mater. Horiz.* **6**, 1409–1415 (2019).
48. San Roman, D. et al. Engineering three-dimensional (3D) out-of-plane graphene edge sites for highly selective two-electron oxygen reduction electrocatalysis. *ACS Catal.* **10**, 1993–2008 (2020).
49. Deng, H. et al. Active sites for oxygen reduction reaction on nitrogen-doped carbon nanotubes derived from polyaniline. *Carbon* **112**, 219–229 (2017).
50. Gao, K. et al. Efficient metal-free electrocatalysts from N-doped carbon nanomaterials: mono-doping and co-doping. *Adv. Mater.* **31**, 1804694 (2019).
51. Fan, M. et al. N-B-OH site-activated graphene quantum dots for boosting electrochemical hydrogen peroxide production. *Adv. Mater.* **35**, e2209086 (2023).
52. Li, H. et al. Analysis of the limitations in the oxygen reduction activity of transition metal oxide surfaces. *Nat. Catal.* **4**, 463–468 (2021).
53. Yang, N. et al. Modulating the oxygen reduction activity of heteroatom-doped carbon catalysts via the triple effect: charge, spin density and ligand effect. *Chem. Sci.* **9**, 5795–5804 (2018).
54. Kim, H. et al. On the mechanism of enhanced oxygen reduction reaction in nitrogen-doped graphene nanoribbons. *Phys. Chem. Chem. Phys.* **13**, 17505–17510 (2011).
55. Ikeda, T. et al. Possible oxygen reduction reactions for graphene edges from first principles. *J. Phys. Chem. C* **118**, 17616–17625 (2014).
56. Li, M. et al. N-doped graphene as catalysts for oxygen reduction and oxygen evolution reactions: theoretical considerations. *J. Catal.* **314**, 66–72 (2014).
57. Lee, B.-H. et al. Supramolecular tuning of supported metal phthalocyanine catalysts for hydrogen peroxide electrosynthesis. *Nat. Catal.* **6**, 234–243 (2023).
58. Jung, E. et al. Atomic-level tuning of Co–N–C catalyst for high-performance electrochemical H₂O₂ production. *Nat. Mater.* **19**, 436–442 (2020).
59. Shao, F. et al. In situ spectroelectrochemical probing of CO redox landscape on copper single-crystal surfaces. *Proc. Natl. Acad. Sci. USA* **119**, e2118166119 (2022).
60. Peng, W. et al. Facilitating two-electron oxygen reduction with pyrrolic nitrogen sites for electrochemical hydrogen peroxide production. *Nat. Commun.* **14**, 4430 (2023).
61. Zhao, X. et al. Unveiling the active structure of single nickel atom catalysis: critical roles of charge capacity and hydrogen bonding. *J. Am. Chem. Soc.* **142**, 5773–5777 (2020).
62. Dong, K. et al. Honeycomb carbon nanofibers: a superhydrophilic O₂-trapping electrocatalyst enables ultrahigh mass activity for the two-electron oxygen reduction reaction. *Angew. Chem. Int. Ed.* **60**, 10583–10587 (2021).
63. Pan, Y. et al. Construction of N, P co-doped carbon frames anchored with Fe single atoms and Fe₂P nanoparticles as a robust coupling catalyst for electrocatalytic oxygen reduction. *Adv. Mater.* **34**, e2203621 (2022).
64. Li, X. et al. Identification of the electronic and structural dynamics of catalytic centers in single-Fe-atom material. *Chem* **6**, 3440–3454 (2020).
65. Yang, C. et al. Interfacial O₂ accumulation affects microenvironment in carbon-based electrocatalysts for H₂O₂ production. *ACS Energy Lett.* **7**, 4398–4407 (2022).
66. Dong, J.-C. et al. In situ Raman spectroscopic evidence for oxygen reduction reaction intermediates at platinum single-crystal surfaces. *Nat. Energy* **4**, 60–67 (2019).
67. Ze, H. et al. Molecular insight of the critical role of Ni in Pt-based nanocatalysts for improving the oxygen reduction reaction probed using an in situ SERS borrowing strategy. *J. Am. Chem. Soc.* **143**, 1318–1322 (2021).
68. Wang, Y.-H. et al. In situ Raman spectroscopy reveals the structure and dissociation of interfacial water. *Nature* **600**, 81–85 (2021).
69. Li, C.-Y. et al. In situ probing electrified interfacial water structures at atomically flat surfaces. *Nat. Mater.* **18**, 697–701 (2019).
70. Wang, Y.-H. et al. Characterizing surface-confined interfacial water at graphene surface by in situ Raman spectroscopy. *Joule* **7**, 1652–1662 (2023).
71. Wei, J. et al. Probing the oxygen reduction reaction intermediates and dynamic active site structures of molecular and pyrolyzed Fe–N–C electrocatalysts by in situ Raman spectroscopy. *ACS Catal.* **12**, 7811–7820 (2022).
72. Diaz-Morales, O. et al. The importance of nickel oxyhydroxide deprotonation on its activity towards electrochemical water oxidation. *Chem. Sci.* **7**, 2639–2645 (2016).
73. Zhu, X. et al. When graphitic nitrogen meets pentagons: selective construction and spectroscopic evidence for improved four-electron oxygen reduction electrocatalysis. *Adv. Mater.* **36**, 2414976 (2025).

74. Xie, L. et al. Isomerization engineering of oxygen-enriched carbon quantum dots for efficient electrochemical hydrogen peroxide production. *Small* **20**, 2401253 (2024).
75. Hu, J. et al. Uncovering dynamic edge-sites in atomic Co-N-C electrocatalyst for selective hydrogen peroxide production. *Angew. Chem. Int. Ed.* **62**, e202304754 (2023).
76. Vojvodic, A. et al. Electronic structure effects in transition metal surface chemistry. *Top. Catal.* **57**, 25–32 (2014).
77. Hammer, B. et al. Why gold is the noblest of all the metals. *Nature* **376**, 238–240 (1995).
78. Greiner, M. T. et al. Free-atom-like *d* states in single-atom alloy catalysts. *Nat. Chem.* **10**, 1008–1015 (2018).
79. Bhattacharjee, S. et al. Cooperation and competition between magnetism and chemisorption. *Phys. Chem. Chem. Phys.* **23**, 3802–3809 (2021).
80. Bhattacharjee, S. et al. Insights into heterogeneous catalysis on surfaces with 3D transition metals: spin-dependent chemisorption models and magnetic field effects. *J. Phys. Chem. Lett.* **14**, 8755–8764 (2023).
81. Cao, A. et al. Spin effects in chemisorption and catalysis. *ACS Catal.* **13**, 3456–3462 (2023).
82. Liu, K. et al. Insights into the activity of single-atom Fe-NC catalysts for oxygen reduction reaction. *Nat. Commun.* **13**, 2075 (2022).
83. Sun, Y. et al. Activity-selectivity trends in the electrochemical production of hydrogen peroxide over single-site metal-nitrogen-carbon catalysts. *J. Am. Chem. Soc.* **141**, 12372–12381 (2019).
84. Han, L. et al. In-plane carbon lattice-defect regulating electrochemical oxygen reduction to hydrogen peroxide production over nitrogen-doped graphene. *ACS Catal.* **9**, 1283–1288 (2019).
85. Shinagawa, T. et al. Insight on Tafel slopes from a microkinetic analysis of aqueous electrocatalysis for energy conversion. *Sci. Rep.* **10**, 6899 (2020).

Acknowledgements

The authors acknowledge the National Science Fund for Excellent Young Scholars (Grant No. 52322607 to F.S.) and the National Natural Science Foundation of China (Grant No. U21A20143 to J.G. and 52076057 to F.S.). The authors acknowledge Beijing PARATERA Tech CO., Ltd. For providing HPC resources that have contributed to the research results reported within this paper. URL: <https://paratera.com/>.

Author contributions

F.S. conceived and supervised the project. F.S. and C.Y. designed and analyzed the experiments. F.S. and C.Y. wrote and revised the paper.

C.Y. and Z.Q. conducted the theoretical calculations and simulations. Y.Z., J.Z., W.Z., J.G., S.L., and Y.L. contributed to the scientific discussion and data interpretation. All authors have read and approved the final manuscript.

Competing interests

The authors declare no competing interests.

Additional information

Supplementary information The online version contains supplementary material available at <https://doi.org/10.1038/s41467-025-66161-5>.

Correspondence and requests for materials should be addressed to Fei Sun.

Peer review information *Nature Communications* thanks the anonymous reviewers for their contribution to the peer review of this work. A peer review file is available.

Reprints and permissions information is available at <http://www.nature.com/reprints>

Publisher's note Springer Nature remains neutral with regard to jurisdictional claims in published maps and institutional affiliations.

Open Access This article is licensed under a Creative Commons Attribution-NonCommercial-NoDerivatives 4.0 International License, which permits any non-commercial use, sharing, distribution and reproduction in any medium or format, as long as you give appropriate credit to the original author(s) and the source, provide a link to the Creative Commons licence, and indicate if you modified the licensed material. You do not have permission under this licence to share adapted material derived from this article or parts of it. The images or other third party material in this article are included in the article's Creative Commons licence, unless indicated otherwise in a credit line to the material. If material is not included in the article's Creative Commons licence and your intended use is not permitted by statutory regulation or exceeds the permitted use, you will need to obtain permission directly from the copyright holder. To view a copy of this licence, visit <http://creativecommons.org/licenses/by-nc-nd/4.0/>.

© The Author(s) 2025